A NEW STICKY PARTICLE METHOD FOR PRESSURELESS GAS DYNAMICS[*]

ALINA CHERTOCK[†], ALEXANDER KURGANOV[‡], AND YURII RYKOV[§]

Abstract. We first present a new sticky particle method for the system of pressureless gas dynamics. The method is based on the idea of sticky particles, which seems to work perfectly well for the models with point mass concentrations and strong singularity formations. In this method, the solution is sought in the form of a linear combination of δ-functions, whose positions and coefficients represent locations, masses, and momenta of the particles, respectively. The locations of the particles are then evolved in time according to a system of ODEs, obtained from a weak formulation of the system of PDEs. The particle velocities are approximated in a special way using global conservative piecewise polynomial reconstruction technique over an auxiliary Cartesian mesh. This velocities correction procedure leads to a desired interaction between the particles and hence to clustering of particles at the singularities followed by the merger of the clustered particles into a new particle located at their center of mass. The proposed sticky particle method is then analytically studied. We show that our particle approximation satisfies the original system of pressureless gas dynamics in a weak sense, but only within a certain residual, which is rigorously estimated. We also explain why the relevant errors should diminish as the total number of particles increases. Finally, we numerically test our new sticky particle method on a variety of one- and two-dimensional problems as well as compare the obtained results with those computed by a high-resolution finite-volume scheme. Our simulations demonstrate the superiority of the results obtained by the sticky particle method that accurately tracks the evolution of developing discontinuities and does not smear the developing δ-shocks.

Key words. nonstrictly hyperbolic systems, conservation laws, pressureless gas dynamics, mass concentration, strong singularities, δ-shock, sticky particle method

AMS subject classifications. 65M25, 65M12, 35L65, 35L67

DOI. 10.1137/050644124

1. Introduction. We consider the Euler equations of pressureless gas dynamics:

$$(1.1) \qquad \mathbf{w}_t + \nabla_{\mathbf{x}} \cdot (\mathbf{u} \otimes \mathbf{w}) = \mathbf{0}.$$

Here, $\mathbf{x} := (x, y, \ldots)$ is an n-dimensional vector of spatial variables, $\mathbf{u} := (u, v, \ldots)$ is the corresponding velocity vector, and $\mathbf{w} \equiv (w^1, w^2, w^3, \ldots)^T := (\rho, \rho u, \rho v, \ldots)^T$ is the $(n+1)$-dimensional vector of unknown function, where ρ is the density.

This system arises in the modeling of the formation of large-scale structures in the universe [24]. It can be formally obtained as the limit of the isotropic Euler equations of gas dynamics as pressure tends to zero or as the macroscopic limit of a Boltzmann equation when the Maxwellian has zero temperature.

Even in the simplest one-dimensional (1-D) case, the system (1.1), which can be rewritten as

$$(1.2) \qquad \begin{cases} \rho_t + (\rho u)_x = 0, \\ (\rho u)_t + (\rho u^2)_x = 0, \end{cases}$$

is mathematically challenging since it is nonstrictly hyperbolic and its Jacobian is not diagonalizable. For smooth solutions, the system (1.2) is equivalent to

$$(1.3) \qquad \rho_t + (\rho u)_x = 0,$$

$$(1.4) \qquad u_t + uu_x = 0.$$

Notice that (1.4) is the inviscid Burgers equation, which is, in fact, decoupled from (1.3). It is well known that the solution of the initial-value problem associated with (1.4), as long as it stays smooth, can be easily obtained by the method of characteristics. The density ρ can then be determined from (1.3), which becomes a linear transport equation. However, if the initial velocity $u(x, 0)$ is not monotone increasing, the characteristics will intersect within a finite time, and the solution will loose its initial smoothness, and thus it must be understood in a weak sense. As in the general theory of weak solutions of hyperbolic systems of conservation laws, one has to introduce discontinuity lines. Let $x = \xi(t)$ be such a line and assume that the solution accepts finite values $u^{\pm} := u(\xi(t) \pm 0, t)$ and $\rho^{\pm} := \rho(\xi(t) \pm 0, t)$ from both sides of discontinuity. The jumps then must satisfy the Rankine–Hugoniot conditions, namely,

$$\begin{cases} \xi'(t)\,(\rho^+ - \rho^-) = \rho^+ u^+ - \rho^- u^-, \\ \xi'(t)\,(\rho^+ u^+ - \rho^- u^-) = \rho^+ \left(u^+\right)^2 - \rho^- \left(u^-\right)^2. \end{cases}$$

After eliminating ξ' from this system, one obtains $\rho^+ \rho^- \left(u^+ - u^-\right)^2 = 0$, which implies $u^+ = u^-$. Therefore, in order to support the shock discontinuity in the velocity field, the density must have a stronger (than a shock) singularity at $x = \xi'(t)$. Since in the Burgers equation, the characteristic lines impinge each other and thus, as part of the system (1.2), cause a mass concentration at the velocity discontinuity line, resulting in the formation of a δ-type singularity in the density field there.

The two-dimensional (2-D) version of (1.1) reads as

$$(1.5) \qquad \begin{cases} \rho_t + (\rho u)_x + (\rho v)_y = 0, \\ (\rho u)_t + (\rho u^2)_x + (\rho uv)_y = 0, \\ (\rho v)_t + (\rho uv)_x + (\rho v^2)_y = 0. \end{cases}$$

Compared to the 1-D case, solutions of the 2-D system have a similar but essentially more sophisticated mechanism of singularities formation due to the dimensionality factor: strong singularities may now be formed either along surfaces or at separate points (we expect that in the three space dimensions the situation is even more complex). The system (1.5) has been intensively studied at the theoretical level (see, e.g., [2, 4, 6, 7, 8, 20, 21]). However, no more or less complete analytical results concerning the existence and uniqueness of solutions in the 2-D case are available. This is primarily related to the difficulties in the theoretical description of the collision of 2-D shocks. (See section 3.2 for an extensive numerical study of this phenomenon.)

Formation and further evolution of singular shocks, their interactions as well as the emergence of vacuum states, make development of numerical methods for the

system (1.1) a challenging problem. A numerical method based on the movement of a system of particles was introduced in [19]. Several finite-volume [17], kinetic [2, 3, 5], and relaxation [1] methods have been recently proposed. These methods are able to reasonably accurately capture δ-shocks, but their applicability is rather limited, for example, most of these methods do not work well for problems where the velocities change sign in regions where the density varies smoothly, [17].

We develop a simple, efficient, and low-dissipative sticky particle method for pressureless gas dynamics. The derivation of our method is based on a weak formulation of the system (1.5) and can be viewed as a practical implementation of the sticky particle method from [4]. We first approximate $\mathbf{w}$ by a collection of N particles, located at $(x_i^N(t), y_i^N(t))$, $i = 1, \ldots, N$, at time t, and carrying fixed masses and momenta. The particle locations are then evolved according to the corresponding system of ODEs, derived by plugging the particle approximation into a weak form of (1.1). In order to prevent the situation, in which approaching particles simply pass by each other without any interaction (such an undesirable situation is obviously impossible in the 1-D case, but is almost unavoidable in the 2-D case), we divide the computational domain into a set of auxiliary cells and compute the total mass and momentums in each cell. The particle velocities are then approximated using the global conservative piecewise polynomial interpolants of ρ, ρu, and ρv, constructed over an auxiliary Cartesian mesh. This way an interaction of all particles located in the same cell is guaranteed. When the particles get even closer to each other, we unite them into a new particle, located at the center of mass of the original clustered particles. The mass (momentum) of the new particle is simply the sum of the masses (corresponding momenta) of the replaced particles, and the velocities of the new particle are uniquely determined from the conservation requirements. This particle merger procedure results in mass concentration, which is an essential property of pressureless gases.

We would like to note that our 2-D sticky particle method can be extended to any number of space dimensions in a rather straightforward manner. In this paper, we restrict our consideration to the 1-D and 2-D cases only, since, to the best of our knowledge, no analytical results on three-dimensional (3-D) pressureless gas dynamics system are available, and it is therefore hard to set up convincing 3-D numerical experiments.

We test our method on a number of 1-D and 2-D numerical examples, in which we compare the results obtained by the new (nondissipative) sticky particle method and by the (dissipative) second-order central-upwind scheme from [11]. The latter scheme is a high-resolution Godunov-type finite-volume method that belongs to a family of central schemes, which may serve as "black-box" solvers for multidimensional hyperbolic systems of conservation laws. The prototype of modern central schemes is the first-order Lax–Friedrichs scheme [9, 16], which is the most universal method for solving (multidimensional systems of) time-dependent PDEs. However, its excessive numerical dissipation prevents sharp resolution and therefore in practice one has to use higher-order schemes. The first high-resolution nonoscillatory central scheme—the second-order Nessyahu–Tadmor scheme—was proposed in [18]. The amount of numerical dissipation present in projection-evolution central schemes was further reduced by incorporating some more upwinding information on local speeds of propagation into the evolution step [12, 14] (the resulting schemes thus have been referred to as central-upwind schemes) and, more recently, by enhancing the accuracy of the projection step [11, 13]. We note that the only upwinding information required by the central-upwind schemes is the eigenvalues of the Jacobians, and therefore application of these schemes to nonstrictly hyperbolic systems like (1.5) is straightforward.

The paper is organized as follows. We start in section 2 by introducing the new sticky particle method for the system (1.5). We then describe, in section 2.1, the velocity correction procedure and, in section 2.2, an algorithm of the unification of clustering particles. The main analytical result in section 2.3 is Theorem 2.1, where we show that even though our particle solution fails to satisfy (1.1) in a weak sense defined in [21], the relevant errors can be rigorously estimated. We then provide a heuristic justification why these errors tend to zero as $N \to \infty$. We conclude in section 3 with several 1-D and 2-D numerical examples and demonstrate that the new method accurately tracks the evolution of developing discontinuities. We also compare solutions computed by the sticky particle method with the corresponding solutions computed using the second-order semidiscrete central-upwind scheme, developed in [11, 12, 14]. A brief description of the central-upwind scheme for the pressureless gas dynamics system (1.5) is provided in Appendix A.

2. Derivation of the sticky particle method. We consider the system (1.1) subject to the compactly supported (or periodic) initial data,

$$(2.1) \qquad \mathbf{w}(\mathbf{x}, 0) \equiv (\rho(\mathbf{x}, 0), \rho u(\mathbf{x}, 0), \rho v(\mathbf{x}, 0))^T, \quad \mathbf{x} := (x, y)^T,$$

and look for the solution of the initial-value problem (1.1), (2.1) in the particle form,

$$(2.2) \quad \mathbf{w}^N(\mathbf{x}, t) = \sum_{i=1}^N \boldsymbol{\alpha}_i(t) \delta(\mathbf{x} - \mathbf{x}_i^N(t)), \ \mathbf{x}_i^N := (x_i^N, y_i^N)^T, \ \boldsymbol{\alpha}_i = (m_i, m_i u_i, m_i v_i)^T.$$

Here, N is a total number of particles, $\mathbf{x}_i^N(t)$ is the location of the ith particle at time t, and $m_i, m_i u_i$, and $m_i v_i$ are its mass, the x-, and the y-momenta, respectively.

In order to study the particle time evolution, we plug (2.2) into the weak formulation of the system (1.1),

$$(2.3) \qquad \int_0^\infty \iint_{\mathbb{R}^2} \left\{ \mathbf{w}^N \cdot [\boldsymbol{\varphi}_t + u\boldsymbol{\varphi}_x + v\boldsymbol{\varphi}_y] \right\} d\mathbf{x}dt - \iint_{\mathbb{R}^2} \mathbf{w}^N(\mathbf{x}, 0) \cdot \boldsymbol{\varphi}(\mathbf{x}, 0) \, d\mathbf{x} = 0,$$

where $\boldsymbol{\varphi}$ is an arbitrary C_0^1 test function. As a result, (2.3) reduces to

$$(2.4) \ \sum_{i=1}^N \int_0^\infty \boldsymbol{\alpha}_i(t) \cdot \left\{ \boldsymbol{\varphi}_t + u\boldsymbol{\varphi}_x + v\boldsymbol{\varphi}_y \right\} \Bigg|_{(\mathbf{x},t)=(\mathbf{x}_i^N(t),t)} dt - \sum_{i=1}^N \boldsymbol{\alpha}_i(0) \cdot \boldsymbol{\varphi}(\mathbf{x}_i^N(0), 0) = 0,$$

which should be satisfied for any $\boldsymbol{\varphi}$. Evolving particle locations according to the following system of ODEs:

$$(2.5) \qquad \frac{dx_i^N(t)}{dt} = u(\mathbf{x}_i^N(t), t), \quad \frac{dy_i^N(t)}{dt} = v(\mathbf{x}_i^N(t), t), \qquad i = 1, \dots, N,$$

and integrating by parts, we rewrite (2.4) as

$$\sum_{i=1}^N \int_0^\infty \frac{d\boldsymbol{\alpha}_i(t)}{dt} \cdot \boldsymbol{\varphi}(\mathbf{x}_i^N(t), t) \, dt = 0.$$

The last equation implies

$$(2.6) \qquad \frac{d\boldsymbol{\alpha}_i(t)}{dt} = 0, \quad i = 1, \dots, N,$$

that is, the particle weights remain constant in time. Thus, the weights can be determined from the initial conditions, for instance, in the following manner. We divide the computational domain Ω into N subdomains Ω_i, $i = 1, \ldots, N$, and place an ith particle with

$$\boldsymbol{\alpha}_i := \iint\limits_{\Omega_i} \mathbf{w}(\mathbf{x}, 0)\, d\mathbf{x}$$

into the center of Ω_i, denoted by $\mathbf{x}_i^N(0) \equiv (x_i^N(0), y_i^N(0))$, which will serve as initial data for the ODE system (2.5).

2.1. Particle velocities. In order to be able to solve the system of ODEs (2.5), one would need to recover the particle velocities at any given time moment. The simplest (and the least dissipative) way to compute the velocities is to divide the corresponding particle momenta by its mass, that is, by taking

$$(2.7) \qquad u_i \equiv u(\mathbf{x}_i^N(t), t) := \frac{m_i u_i}{m_i}, \quad v_i \equiv v(\mathbf{x}_i^N(t), t) := \frac{m_i v_i}{m_i}.$$

In fact, this means that every particle travels with constant velocity until it collides with another particle (see section 2.2). This approach can be rigorously justified through the weak formulation (2.3) and it seems to work perfectly in the 1-D case, in which collision of approaching particles is unavoidable. However, in the 2-D case, the probability of collision of two particles approaching the same singularity curve is zero unless a special symmetry in initial particle locations has been imposed (see Example 5 in section 3.2).

We propose an alternative way of particle velocities reconstruction, which is independent of an initial placement of particles. Our approach is based on a global piecewise polynomial reconstruction technique, which is widely used in finite-volume framework (see Appendix A and the references therein). To adopt this technique to a mesh-free particle method we introduce an auxiliary Cartesian grid (which may vary in time). The grid should be adapted to the particle distribution so that the number of particles in every cell is about the same. In our numerical experiments, we have used the simplest strategy: we have adapted the auxiliary grid to the initial (uniform) particle distribution only by taking the size of the cells to be twice larger than the distance between the particles. A more sophisticated adaptation strategy may lead to more accurate results, but its optimization may substantially increase the complexity of the proposed sticky particle method.

Taking a simple uniform auxiliary grid, $x_j \equiv j\Delta x$, $y_k \equiv k\Delta y$, we first compute the cell averages of the conserved quantities at time t,

$$(2.8) \qquad \bar{\mathbf{w}}_{j,k}(t) = \frac{1}{\Delta x \Delta y} \sum_{i:\, \mathbf{x}_i^N(t) \in I_{j,k}} \boldsymbol{\alpha}_i, \qquad I_{j,k} = [x_{j-\frac{1}{2}}, x_{j+\frac{1}{2}}] \times [y_{k-\frac{1}{2}}, y_{k+\frac{1}{2}}].$$

Using these cell averages, we then reconstruct a nonoscillatory piecewise polynomial interpolant of an appropriate order of accuracy, denoted by

$$\widetilde{\mathbf{w}}(\mathbf{x}, t) := (w^1(\mathbf{x}, t), w^2(\mathbf{x}, t), w^3(\mathbf{x}, t))^T,$$

which is used to compute the particle velocities,

$$(2.9) \qquad u_i := \frac{\widetilde{w}^2(\mathbf{x}_i^N(t), t)}{\widetilde{w}^1(\mathbf{x}_i^N(t), t)}, \quad v_i := \frac{\widetilde{w}^3(\mathbf{x}_i^N(t), t)}{\widetilde{w}^1(\mathbf{x}_i^N(t), t)}.$$

Notice that in order to ensure that no mass (momentum) is artificially lost (created) at this step, the reconstruction must be performed in a conservative manner, namely, one should guarantee that

$$\sum_{i:\,\mathbf{x}_i^N(t)\in I_{j,k}} \widetilde{\mathbf{w}}(\mathbf{x}_i^N(t),t) = \bar{\mathbf{w}}_{j,k}(t).$$

We achieve the conservation (in fact, while the mass is conserved exactly, only approximate momentum conservation is guaranteed; see the computation in section 2.3) by taking $\widetilde{\mathbf{w}}$ to be a second-order accurate piecewise linear reconstruction centered at the center of mass of the particles located in the $I_{j,k}$ cell,

$$
\begin{aligned}
\widetilde{\mathbf{w}}(x,y,t) = \bar{\mathbf{w}}_{j,k} &+ (\mathbf{s}_x)_{j,k}(x - x_{j,k}^{\mathrm{CM}}(t)) \\
&+ (\mathbf{s}_y)_{j,k}(y - y_{j,k}^{\mathrm{CM}}(t)) \ \ \text{for} \ \ (x,y)\in I_{j,k},
\end{aligned}
\tag{2.10}
$$

where the coordinates of the center of mass are

$$
x_{j,k}^{\mathrm{CM}}(t) := \frac{\displaystyle\sum_{i:\,\mathbf{x}_i^N(t)\in I_{j,k}} m_i x_i^N(t)}{\displaystyle\sum_{i:\,\mathbf{x}_i^N(t)\in I_{j,k}} m_i}, \quad
y_{j,k}^{\mathrm{CM}}(t) := \frac{\displaystyle\sum_{i:\,\mathbf{x}_i^N(t)\in I_{j,k}} m_i y_i^N(t)}{\displaystyle\sum_{i:\,\mathbf{x}_i^N(t)\in I_{j,k}} m_i},
\tag{2.11}
$$

and the slopes $(\mathbf{s}_x)_{j,k}$ and $(\mathbf{s}_y)_{j,k}$ are (at least) first-order approximations of the derivatives $\mathbf{w}_x(x_{j,k}^{\mathrm{CM}}(t), y_{j,k}^{\mathrm{CM}}(t))$ and $\mathbf{w}_y(x_{j,k}^{\mathrm{CM}}(t), y_{j,k}^{\mathrm{CM}}(t))$, respectively.

Finally, in order to ensure a nonoscillatory nature of the reconstruction (2.10), the slopes $(\mathbf{s}_x)_{j,k}$ and $(\mathbf{s}_y)_{j,k}$ should be computed using a nonlinear limiter. In our numerical experiments, we have used the minmod limiter applied in the following way.

Let us take, for example, the first component of $\mathbf{w}$ (density) and consider the four planes, denoted by $\pi_{j,k}^{\mathrm{NE}}, \pi_{j,k}^{\mathrm{NW}}, \pi_{j,k}^{\mathrm{SE}}, \pi_{j,k}^{\mathrm{SW}}$, that pass through the following four triplets of points:

$$
\pi_{j,k}^{\mathrm{NE}}: \left\{(x_{j,k}^{\mathrm{CM}}, y_{j,k}^{\mathrm{CM}}, \bar{w}_{j,k}^1), (x_{j,k+1}^{\mathrm{CM}}, y_{j,k+1}^{\mathrm{CM}}, \bar{w}_{j,k+1}^1), (x_{j+1,k}^{\mathrm{CM}}, y_{j+1,k}^{\mathrm{CM}}, \bar{w}_{j+1,k}^1)\right\},
$$

$$
\pi_{j,k}^{\mathrm{NW}}: \left\{(x_{j,k}^{\mathrm{CM}}, y_{j,k}^{\mathrm{CM}}, \bar{w}_{j,k}^1), (x_{j,k+1}^{\mathrm{CM}}, y_{j,k+1}^{\mathrm{CM}}, \bar{w}_{j,k+1}^1), (x_{j-1,k}^{\mathrm{CM}}, y_{j-1,k}^{\mathrm{CM}}, \bar{w}_{j-1,k}^1)\right\},
$$

$$
\pi_{j,k}^{\mathrm{SE}}: \left\{(x_{j,k}^{\mathrm{CM}}, y_{j,k}^{\mathrm{CM}}, \bar{w}_{j,k}^1), (x_{j,k-1}^{\mathrm{CM}}, y_{j,k-1}^{\mathrm{CM}}, \bar{w}_{j,k-1}^1), (x_{j+1,k}^{\mathrm{CM}}, y_{j+1,k}^{\mathrm{CM}}, \bar{w}_{j+1,k}^1)\right\},
$$

$$
\pi_{j,k}^{\mathrm{SW}}: \left\{(x_{j,k}^{\mathrm{CM}}, y_{j,k}^{\mathrm{CM}}, \bar{w}_{j,k}^1), (x_{j,k-1}^{\mathrm{CM}}, y_{j,k-1}^{\mathrm{CM}}, \bar{w}_{j,k-1}^1), (x_{j-1,k}^{\mathrm{CM}}, y_{j-1,k}^{\mathrm{CM}}, \bar{w}_{j-1,k}^1)\right\}
\tag{2.12}
$$

(the dependence of $\{x_{j,k}^{\mathrm{CM}}\}$ and $\{y_{j,k}^{\mathrm{CM}}\}$ on t has been omitted here for briefness). We then denote the gradients of these planes by $((\pi_x)_{j,k}^{\mathrm{NE}}, (\pi_y)_{j,k}^{\mathrm{NE}})^T$, $((\pi_x)_{j,k}^{\mathrm{NW}}, (\pi_y)_{j,k}^{\mathrm{NW}})^T$, etc., and take the first component of the slopes in (2.10) to be

$$
(s_x^1)_{j,k} = \mathrm{minmod}\left((\pi_x)_{j,k}^{\mathrm{NE}}, (\pi_x)_{j,k}^{\mathrm{NW}}, (\pi_x)_{j,k}^{\mathrm{SE}}, (\pi_x)_{j,k}^{\mathrm{SW}}\right),
$$

$$
(s_y^1)_{j,k} = \mathrm{minmod}\left((\pi_y)_{j,k}^{\mathrm{NE}}, (\pi_y)_{j,k}^{\mathrm{NW}}, (\pi_y)_{j,k}^{\mathrm{SE}}, (\pi_y)_{j,k}^{\mathrm{SW}}\right),
\tag{2.13}
$$

where the minmod function is defined by

$$(2.14) \qquad \mathrm{minmod}(c_1, c_2, \ldots) := \begin{cases} \min(c_1, c_2, \ldots) & \text{if } c_i > 0 \ \forall i, \\ \max(c_1, c_2, \ldots) & \text{if } c_i < 0 \ \forall i, \\ 0 & \text{otherwise.} \end{cases}$$

The reconstructions for the other two fields of $\mathbf{w}$ (momenta) are obtained in a similar way.

   Remarks.
   1. It may happen that one of the planes in (2.12) is perpendicular to the (x, y)-plane or is not uniquely determined. Then this plane is not taken into account, and its gradient is excluded from the formulae for the slopes in (2.13).
   2. As was mentioned in section 1, our velocity recovery procedure ensures that there is an interaction between the particles, located inside the same auxiliary grid cell. As is illustrated in our numerical experiments (see section 3.2), this leads to the desired clustering of particles at the singularities.

2.2. Unification of clustering particles. A major drawback of particle methods is that, in general, their resolution and efficiency significantly deteriorate when too many particles cluster near the same point at the singularity. To prevent such an undesired situation, we unite clustering particles according to the following algorithm. We choose a certain critical distance d_{cr} and as soon as the distance between any two particles gets smaller than the critical distance, we unite them into a new "heavier" particle.

Let us assume that at some time t, the distance between the ith and the jth particles, $|\mathbf{x}_i(t) - \mathbf{x}_j(t)|$, is smaller than d_{cr}. We then replace these two particles with a new one of the following total mass and momenta:

$$(2.15) \qquad \boldsymbol{\alpha}_{\mathrm{new}} = \boldsymbol{\alpha}_i + \boldsymbol{\alpha}_j,$$

located at the center of mass of the replaced particles, namely,

$$(2.16) \qquad \mathbf{x}_{\mathrm{new}}^N = \frac{m_i \mathbf{x}_i^N + m_j \mathbf{x}_j^N}{m_i + m_j}.$$

The velocities of the new particle are determined according to the procedure in section 2.1. After completing the replacement process (2.15)–(2.16), we check whether any other two particles are to be united, and if not, the remaining set of particles is further evolved in time according to (2.2), (2.5), (2.9) until another particle clustering occurs. Then, the unification procedure is repeated, and so forth.

   Remark. The critical distance d_{cr} should be chosen experimentally. In all our numerical examples, except for Example 4, this distance was taken a quarter of a minimal initial distance between the particles (note that the initial distribution of particles is rather uniform in every numerical example below). In Example 4, d_{cr} was made proportional to the size of the shrinking support of the solution.

   We would also like to stress that our numerical experiments clearly indicate that the presented sticky particle method does not seem to be sensitive to the choice of d_{cr}.

2.3. On convergence of the sticky particle method. In previous sections, a sequence of approximate solutions $\{\mathbf{w}^N\}_{N=1}^\infty$ of the system (1.1) for a fixed time interval $[0, T]$ has been constructed based on the dynamics of moving particles. In this section, we show that the measures $\mathbf{w}^N$ do not satisfy (1.1) in a weak sense.

Nevertheless, in Theorem 2.1, we obtain rigorous estimates for relevant errors and further discuss the heuristic justification why these errors tend to zero as $N \to \infty$.

In order to exactly formulate the theorem, let us first describe the interactions of moving particles in detail. Consider a time interval $[t_1, t_2] \subset [0, T]$, some number p of moving particles, and a time moment t_0 such that the particles evolve according to the ODE system (2.5)–(2.6) for $t \in [t_1, t_0)$ and $t \in (t_0, t_2]$, while at time t_0 the particles either coalesce (Case I) or change the velocities according to (2.9) (Case II).

For the considered group of p particles, $\mathcal{P}$, with the total mass

$$M := \sum_{i \in \mathcal{P}} m_i,$$

we introduce the following notation.
- Prior to $t = t_0$ we denote by
  $\boldsymbol{\alpha}_i = (m_i, m_i u_i, m_i v_i)^T$: weights of the particles,
  $(x_i(t), y_i(t))$: their locations at time $t < t_0$,
  $(x_i^0, y_i^0) = (x_i(t_0), y_i(t_0))$: final locations of the particles at time $t = t_0$.
- At $t = t_0$ the considered p particles either
  − coalesce (Case I) and then we denote by
  $\boldsymbol{\alpha} = (M, MU, MV)$: weights of the newly formed particle of mass M,
  $U = \dfrac{\sum_{i \in \mathcal{P}} m_i u_i}{\sum_{i \in \mathcal{P}} m_i}$ and $V = \dfrac{\sum_{i \in \mathcal{P}} m_i v_i}{\sum_{i \in \mathcal{P}} m_i}$: its x- and y-velocities,
  $(X_0, Y_0) = (X(t_0), Y(t_0))$: its initial position at time $t = t_0$,
  $(X(t), Y(t))$: its location at time $t > t_0$;
  or
  − undergo the velocities correction (Case II) and then we denote by
  $\widetilde{\boldsymbol{\alpha}}_i = (m_i, m_i \widetilde{u}_i, m_i \widetilde{v}_i)^T$: new weights of the original p particles,
  $(x_i(t), y_i(t))$: their locations, which are not instantaneously affected by the velocities correction procedure and thus change continuously.

We also denote by $\left(x^{\mathrm{CM}}(t), y^{\mathrm{CM}}(t)\right)$ the location of the center of mass of the considered group of p particles,

$$(2.17) \qquad x^{\mathrm{CM}}(t) = \frac{\sum\limits_{i \in \mathcal{P}} m_i x_i(t)}{\sum\limits_{i \in \mathcal{P}} m_i}, \quad y^{\mathrm{CM}}(t) = \frac{\sum\limits_{i \in \mathcal{P}} m_i y_i(t)}{\sum\limits_{i \in \mathcal{P}} m_i}.$$

Let us call by *the event with respect to Case* I the situation when some number of particles coalesce at some time moment and at some location. Suppose E_{C1} is the set of such events, and denote by N_{C1} the number of such events that take place in the computational domain within the specified time interval. It is obvious that, in general, N_{C1} is less than the initial number of particles N since each possible merging reduces the number of particles by, at least, one.

Let us call by *the event with respect to Case* II the situation when the velocities of a particle change according to (2.9) at some time moment. Suppose E_{C2} is the set of such events, and denote by N_{C2} the number of such events that take place in the computational domain within the specified time interval. Notice that all existing particles, whose total number is always less or equal to N, can undergo the velocity correction procedure at every time step. The minimal distance between the particles is controlled by the particle unification procedure and is thus proportional to $1/\sqrt{N}$. Due to the CFL condition, the size of each time step is proportional to the minimal

distance between the particles. Therefore, the total number of time steps in our 2-D sticky particle method is proportional to $\sqrt{N}$, and hence $N_{\mathrm{C2}} \lesssim N^{3/2}$.

We are now ready to formulate the following theorem.

THEOREM 2.1. *Let $\mathbf{R}$ be the residual of the particle solution $\mathbf{w}^N$, that is, let $\mathbf{w}^N$ satisfies the equation*

$$\mathbf{w}_t + (u\mathbf{w})_x + (v\mathbf{w})_y = \mathbf{R}(x, y, z)$$

in the weak sense defined in [21, Definition 1] for any time interval $[t_1, t_2] \subset [0, T]$.

If the slopes $(\mathbf{s}_x)_{j,k}$ and $(\mathbf{s}_y)_{j,k}$ in the piecewise linear reconstruction (2.9) are set to be 0 in all cells $I_{j,k}$, then the size of the residual can be estimated by

$$(2.18) \quad |\mathbf{R}| \le C\varepsilon \sum_{E_{\mathrm{C1}} \cup E_{\mathrm{C2}}} \left(\frac{\sum\limits_{i<l} m_i m_l \left(|u_i - u_l| + |v_i - v_l| \right)}{\sum\limits_{l} m_l} + \varepsilon \sum_i m_i \left(1 + |u_i| + |v_i| \right) \right),$$

where the summation is taken over the particles that participate in the specific event from E_{C1} or E_{C2}, and $\varepsilon := \sqrt{(\Delta x)^2 + (\Delta y)^2}$ is the diameter of the auxiliary grid cell, which is assumed to tend to 0 as $N \to \infty$.

In the case the slopes $(\mathbf{s}_x)_{j,k}$ and $(\mathbf{s}_y)_{j,k}$ in (2.9) are defined according to formulae (2.10)–(2.12), the estimate (2.18) is also true provided the following bound

$$(2.19) \qquad \left| (s_x^r)_{j,k} \left(x_i - x_{j,k}^{\mathrm{CM}} \right) + (s_y^r)_{j,k} \left(y_i - y_{j,k}^{\mathrm{CM}} \right) \right| \le C\varepsilon \bar{w}_{j,k}^r, \quad r = 1, 2, 3,$$

is true at each auxiliary $I_{j,k}$ cell and for each particle such that $(x_i, y_i) \in I_{j,k}$. Here, $x_{j,k}^{\mathrm{CM}}$ and $y_{j,k}^{\mathrm{CM}}$, given by (2.11), are the coordinates of the center of mass of the particles, located in $I_{j,k}$ at the time moment when the velocity correction procedure is performed.

Remark. The conditions (2.19) are rather technical. It is clear that for the reconstruction (2.10)–(2.14) they hold in smooth parts of the solution (away from vacuum), where all the slopes are bounded. In the nonsmooth parts of the solution and near vacuum, the conditions (2.19) represent a certain nonoscillatory requirement, which may or may not be satisfied by the reconstruction (2.10)–(2.14).

Proof. We start by observing that there is a finite number (which may be proportional to N) of time moments in the interval $[0, T]$ at which some particle velocities change according to either Case I or Case II. Therefore, it is enough to consider such time intervals $[t_1, t_2]$ that contain only a single moment $t = t_0$ of the velocities change.

Let us next fix a test function, $\boldsymbol{\psi} \equiv (\psi^1, \psi^2, \psi^3)^T \in C_0^1(\mathbb{R}^2)$ and consider the following two sets of time moments:

$$\mathcal{T}_1 := \{ t_{1_i} \in [t_1, t_0], i = 1, \ldots, q_1 \} \quad \text{and} \quad \mathcal{T}_2 := \{ t_{2_i} \in [t_0, t_2], i = 1, \ldots, q_2 \},$$

such that some particle either enters or leaves the domain

$$(2.20) \qquad\qquad\qquad \Phi := \operatorname{supp} \psi^1 \cup \operatorname{supp} \psi^2 \cup \operatorname{supp} \psi^3$$

at these times.

Notice that it suffices to consider the sets $\mathcal{T}_1$ and $\mathcal{T}_2$ to be finite. If not, then the supports of functions ψ^i, $i = 1, 2, 3$, can be placed into larger convex sets Λ_i and the functions ψ^i can be extended to Λ_i by zero. As has been mentioned above, there is only a finite number of time moments in the interval $[0, T]$ at which some particle velocities change according to either Case I or Case II. Between these time moments

all the particles freely move along straight lines and, due to the convexity of Λ_i, they can intersect the boundaries of Λ_i at most twice. Therefore, replacing $\operatorname{supp}\psi^i$ with Λ_i in (2.20) will make $\mathcal{T}_1$ and $\mathcal{T}_2$ finite.

The conservation laws are thus satisfied in any time interval $[t_{1_i}, t_{1_{i+1}}]$ or $[t_{2_k}, t_{2_{k+1}}]$ since no velocities correction procedures are performed and since the test function ψ vanishes at the points where particles enter or leave the domain Φ. Hence, it is enough to consider only the particles dynamics in the time interval $[\max_i t_{1_i}, \min_k t_{2_k}]$, such that at time $t = \max_i t_{1_i}$ there are p particles (from $\mathcal{P}$) inside the domain Φ and no particles enter or leave Φ until $t = \min_k t_{2_k}$. In order to simplify the notation, we again denote such interval by $[t_1, t_2]$.

Case I. First, we suppose that the particle formed at the time moment $t = t_0$ stays inside the domain Φ. We then plug the particle solution (2.2) into the weak formulation (in the sense of [21, Definition 1]) of (1.1) over the time interval $[t_1, t_2]$ to compute the residuals for the equations of mass and momenta conservation.

• From the *mass conservation* equation we obtain

$$\int_{t_1}^{t_0} \left\{ \sum_{i\in\mathcal{P}} \left[\psi_x^1(x_i(\tau), y_i(\tau)) m_i u_i + \psi_y^1(x_i(\tau), y_i(\tau)) m_i v_i \right] \right\} d\tau$$

$$+ \int_{t_0}^{t_2} \left\{ \psi_x^1(X(\tau), Y(\tau)) MU + \psi_y^1(X(\tau), Y(\tau)) MV \right\} d\tau$$

$$= \int_{t_1}^{t_0} \frac{d}{d\tau} \sum_{i\in\mathcal{P}} m_i \psi^1(x_i(\tau), y_i(\tau)) \, d\tau + \int_{t_0}^{t_2} \frac{d}{d\tau} M\psi^1(X(\tau), Y(\tau)) \, d\tau$$

$$= M\psi^1(X(t_2), Y(t_2)) - \sum_{i\in\mathcal{P}} m_i \psi^1(x_i(t_1), y_i(t_1)) + R^1,$$

where

(2.21) $$R^1 = \sum_{i\in\mathcal{P}} m_i \psi^1(x_i^0, y_i^0) - M\psi^1(X_0, Y_0).$$

Rewriting (2.21), using the Taylor expansion about (X_0, Y_0) and taking into account (2.17) for $t = t_0$, we arrive at

$$R^1 = \sum_{i\in\mathcal{P}} m_i \left[\psi^1(x_i^0, y_i^0) - \psi^1(X_0, Y_0) \right]$$

$$= \sum_{i\in\mathcal{P}} m_i \left[\psi_x^1(X_0, Y_0) \left(x_i^0 - X_0 \right) + \psi_y^1(X_0, Y_0) \left(y_i^0 - Y_0 \right) + \mathcal{O}(\varepsilon^2) \right]$$

$$= \psi_x^1(X_0, Y_0) \left[\sum_{i\in\mathcal{P}} m_i x_i^0 - MX_0 \right] + \psi_y^1(X_0, Y_0) \left[\sum_{i\in\mathcal{P}} m_i y_i^0 - MY_0 \right] + M \cdot \mathcal{O}(\varepsilon^2)$$

(2.22) $$= M \cdot \mathcal{O}(\varepsilon^2).$$

• From the *x-momentum conservation* equation we obtain

$$\int_{t_1}^{t_0} \left\{ \sum_{i\in\mathcal{P}} \left[\psi_x^2(x_i(\tau), y_i(\tau)) u_i \cdot m_i u_i + \psi_y^2(x_i(\tau), y_i(\tau)) v_i \cdot m_i u_i \right] \right\} d\tau$$

$$+ \int_{t_0}^{t_2} \left\{ \psi_x^2(X(\tau), Y(\tau)) U \cdot MU + \psi_y^2(X(\tau), Y(\tau)) V \cdot MU \right\} d\tau$$

$$= \int_{t_1}^{t_0} \frac{d}{d\tau} \sum_{i \in \mathcal{P}} m_i u_i \psi^2(x_i(\tau), y_i(\tau)) \, d\tau + \int_{t_0}^{t_2} \frac{d}{d\tau} MU\psi^2(X(\tau), Y(\tau)) \, d\tau$$

$$= MU\psi^2(X(t_2), Y(t_2)) - \sum_{i \in \mathcal{P}} m_i u_i \psi^2(x_i(t_1), y_i(t_1)) + R^2,$$

where

$$(2.23) \qquad R^2 = \sum_{i \in \mathcal{P}} m_i u_i \psi^2(x_i^0, y_i^0) - MU\psi^2(X_0, Y_0).$$

We now rewrite (2.23) and use the Taylor expansion about (X_0, Y_0) and (2.17) to obtain

$$R^2 = \sum_{i \in \mathcal{P}} m_i u_i \left[\psi^2(x_i^0, y_i^0) - \psi^2(X_0, Y_0) \right]$$

$$= \sum_{i \in \mathcal{P}} m_i u_i \left[\psi_x^2(X_0, Y_0) \left(x_i^0 - X_0 \right) + \psi_y^2(X_0, Y_0) \left(y_i^0 - Y_0 \right) + \mathcal{O}(\varepsilon^2) \right]$$

$$= \psi_x^2(X_0, Y_0) \left[\sum_{i \in \mathcal{P}} m_i u_i x_i^0 - MUX_0 \right] + \psi_y^2(X_0, Y_0) \left[\sum_{i \in \mathcal{P}} m_i u_i y_i^0 - MUY_0 \right] + MU \cdot \mathcal{O}(\varepsilon^2)$$

$$= \psi_x^2(X_0, Y_0) \left[\sum_{i \in \mathcal{P}} m_i u_i x_i^0 - \frac{\sum\limits_{i \in \mathcal{P}} m_i u_i \cdot \sum\limits_{l \in \mathcal{P}} m_l x_l^0}{\sum\limits_{l \in \mathcal{P}} m_l} \right]$$

$$+ \psi_y^2(X_0, Y_0) \left[\sum_{i \in \mathcal{P}} m_i u_i y_i^0 - \frac{\sum\limits_{i \in \mathcal{P}} m_i u_i \cdot \sum\limits_{l \in \mathcal{P}} m_l y_l^0}{\sum\limits_{l \in \mathcal{P}} m_l} \right] + MU \cdot \mathcal{O}(\varepsilon^2).$$

Then, taking into account that

$$\sum_{i \in \mathcal{P}} m_i u_i x_i^0 - \frac{\sum\limits_{i \in \mathcal{P}} m_i u_i \cdot \sum\limits_{l \in \mathcal{P}} m_l x_l^0}{\sum\limits_{l \in \mathcal{P}} m_l} = \frac{\sum\limits_{i,l \in \mathcal{P}} \left(m_l m_i u_i x_i^0 - m_i m_l u_i x_l^0 \right)}{\sum\limits_{l \in \mathcal{P}} m_l}$$

$$= \frac{\sum\limits_{i,l \in \mathcal{P}} m_i m_l u_i \left(x_i^0 - x_l^0 \right)}{\sum\limits_{l \in \mathcal{P}} m_l} = \frac{\sum\limits_{i,l \in \mathcal{P}: i < l} \left[m_i m_l u_i \left(x_i^0 - x_l^0 \right) + m_l m_i u_l \left(x_l^0 - x_i^0 \right) \right]}{\sum\limits_{l \in \mathcal{P}} m_l}$$

$$= \frac{\sum\limits_{i,l \in \mathcal{P}: i < l} m_i m_l \left(x_i^0 - x_l^0 \right) \left(u_i - u_l \right)}{\sum\limits_{l \in \mathcal{P}} m_l},$$

we end up with

$$R^2 = \psi_x^2(X_0, Y_0) \frac{\sum\limits_{i,l \in \mathcal{P}: i < l} m_i m_l (x_i^0 - x_l^0)(u_i - u_l)}{\sum\limits_{l \in \mathcal{P}} m_l}$$

$$(2.24) \qquad + \psi_y^2(X_0, Y_0) \frac{\sum\limits_{i,l \in \mathcal{P}: i < l} m_i m_l (y_i^0 - y_l^0)(u_i - u_l)}{\sum\limits_{l \in \mathcal{P}} m_l} + MU \cdot \mathcal{O}(\varepsilon^2).$$

• In a similar manner, we consider the third component of the residual,

$$(2.25) \qquad R^3 = \sum_{i \in \mathcal{P}} m_i v_i \psi^3(x_i^0, y_i^0) - MV\psi^3(X_0, Y_0),$$

and then from the *y-momentum conservation* equation derive

$$R^3 = \psi_x^3(X_0, Y_0)\frac{\sum\limits_{i,l \in \mathcal{P}: i<l} m_i m_l (x_i^0 - x_l^0)(v_i - v_l)}{\sum\limits_{l \in \mathcal{P}} m_l}$$

$$(2.26) \qquad + \psi_y^3(X_0, Y_0)\frac{\sum\limits_{i,l \in \mathcal{P}: i<l} m_i m_l (y_i^0 - y_l^0)(v_i - v_l)}{\sum\limits_{l \in \mathcal{P}} m_l} + MV \cdot \mathcal{O}(\varepsilon^2).$$

Finally, combining formulae (2.22), (2.24), and (2.26) and using the fact that the distance between (x_i^0, y_i^0) and (x_l^0, y_l^0) is less than $d_{cr} < \varepsilon$, we immediately conclude with the desired estimate (2.18).

Remark. Recall that formulae (2.22), (2.24), and (2.26) were derived under assuming that the particle formed at $t = t_0$ stays inside the domain Φ. If not, then $\boldsymbol{\psi}(X_0, Y_0) = \mathbf{0}$ and all the particles from $\mathcal{P}$ lie within the distance $d_{cr} < \varepsilon$ from the boundary of $\boldsymbol{\psi}$. Thus the estimate (2.18) follows (as can be seen from formulae (2.21), (2.23), and (2.25)) since $\boldsymbol{\psi} \in C_0^1(\mathbb{R}^2)$ and $|\boldsymbol{\psi}(x_i^0, y_i^0)| < C\varepsilon^2$ for all $(x_i^0, y_i^0) \in \mathcal{P}$.

Case II. As in Case I, we plug the particle solution (2.2) into the weak formulation (in the sense of [21, Definition 1]) of (1.1) over the time interval $[t_1, t_2]$ to compute the corresponding residuals. However, since the set of particles participating in the velocities correction procedure at time $t = t_0$, described in section 2.1, coincides (in general) with the set of all existing particles (including the ones lying outside the domain Φ), the residuals computation is carried out as follows.

• From the *mass conservation* equation we obtain

$$\int_{t_1}^{t_0} \left\{ \sum_{i \in \mathcal{P}} \left[\psi_x^1(x_i(\tau), y_i(\tau))m_i u_i + \psi_y^1(x_i(\tau), y_i(\tau))m_i v_i \right] \right\} d\tau$$

$$+ \int_{t_0}^{t_2} \left\{ \sum_{i \in \mathcal{P}} \left[\psi_x^1(x_i(\tau), y_i(\tau))m_i \widetilde{u}_i + \psi_y^1(x_i(\tau), y_i(\tau))m_i \widetilde{v}_i \right] \right\} d\tau$$

$$= \int_{t_1}^{t_0} \frac{d}{d\tau} \sum_{i \in \mathcal{P}} m_i \psi^1(x_i(\tau), y_i(\tau)) \, d\tau + \int_{t_0}^{t_2} \frac{d}{d\tau} \sum_{i \in \mathcal{P}} m_i \psi^1(x_i(\tau), y_i(\tau)) \, d\tau$$

$$= \sum_{i \in \mathcal{P}} m_i \psi^1(x_i(t_2), y_i(t_2)) - \sum_{i \in \mathcal{P}} m_i \psi^1(x_i(t_1), y_i(t_1)).$$

Unlike Case I, the particle trajectories are now continuous within the time interval $[t_1, t_2]$ because only particle velocities may change at $t = t_0$. Therefore, the first component of the residual is

$$(2.27) \qquad R^1 = \sum_{i \in \mathcal{P}} m_i \psi^1(x_i^0, y_i^0) - \sum_{i \in \mathcal{P}} m_i \psi^1(x_i^0, y_i^0) = 0.$$

• From the *x-momentum conservation* equation we obtain

$$\int_{t_1}^{t_0} \left\{ \sum_{i \in \mathcal{P}} \left[\psi_x^2(x_i(\tau), y_i(\tau))u_i \cdot m_i u_i + \psi_y^2(x_i(\tau), y_i(\tau))v_i \cdot m_i u_i \right] \right\} d\tau$$

$$+ \int_{t_0}^{t_2} \left\{ \sum_{i \in \mathcal{P}} \left[\psi_x^2(x_i(\tau), y_i(\tau)) \widetilde{u}_i \cdot m_i \widetilde{u}_i + \psi_y^2(x_i(\tau), y_i(\tau)) \widetilde{v}_i \cdot m_i \widetilde{u}_i \right] \right\} d\tau$$

$$= \int_{t_1}^{t_0} \frac{d}{d\tau} \sum_{i \in \mathcal{P}} m_i u_i \psi^2(x_i(\tau), y_i(\tau)) \, d\tau + \int_{t_0}^{t_2} \frac{d}{d\tau} \sum_{i \in \mathcal{P}} m_i \widetilde{u}_i \psi^2(x_i(\tau), y_i(\tau)) \, d\tau$$

$$= \sum_{i \in \mathcal{P}} m_i \widetilde{u}_i \psi^2(x_i(t_2), y_i(t_2)) - \sum_{i \in \mathcal{P}} m_i u_i \psi^2(x_i(t_1), y_i(t_1)) + R^2,$$

where

$$(2.28) \qquad R^2 = \sum_{i \in \mathcal{P}} \psi^2(x_i^0, y_i^0)(m_i u_i - m_i \widetilde{u}_i).$$

Note that the summation in (2.28) is taken over the particles located in the domain Φ, which consists of a certain number of auxiliary cells (or their parts) $I_{j,k}$. Thus, the residual R^2 can be written as the sum of residuals in each cell $I_{j,k}$ that contains (at least one) particle and has a nonempty intersection with Φ. Let us now consider such a cell, denote the set of particles, located in it at time moment $t = t_0$, by $\mathcal{P}_{j,k}$, and the residual in this cell by $R_{j,k}^2$.

Applying the Taylor expansion about the center of mass $(x_{j,k}^{\mathrm{CM}}, y_{j,k}^{\mathrm{CM}})$ given by (2.11) yields

$$R_{j,k}^2 = \sum_{i \in \mathcal{P}_{j,k}} \left[\psi^2\left(x_{j,k}^{\mathrm{CM}}, y_{j,k}^{\mathrm{CM}}\right) + \psi_x^2\left(x_{j,k}^{\mathrm{CM}}, y_{j,k}^{\mathrm{CM}}\right)\left(x_i^0 - x_{j,k}^{\mathrm{CM}}\right) \right.$$

$$\left. + \psi_y^2\left(x_{j,k}^{\mathrm{CM}}, y_{j,k}^{\mathrm{CM}}\right)\left(y_i^0 - y_{j,k}^{\mathrm{CM}}\right) + \mathcal{O}(\varepsilon^2) \right] m_i(u_i - \widetilde{u}_i)$$

$$= \left[\psi^2\left(x_{j,k}^{\mathrm{CM}}, y_{j,k}^{\mathrm{CM}}\right) + \mathcal{O}(\varepsilon^2) \right] \sum_{i \in \mathcal{P}_{j,k}} m_i(u_i - \widetilde{u}_i)$$

$$+ \psi_x^2\left(x_{j,k}^{\mathrm{CM}}, y_{j,k}^{\mathrm{CM}}\right) \sum_{i \in \mathcal{P}_{j,k}} m_i(u_i - \widetilde{u}_i)\left(x_i^0 - x_{j,k}^{\mathrm{CM}}\right)$$

$$(2.29) \qquad + \psi_y^2\left(x_{j,k}^{\mathrm{CM}}, y_{j,k}^{\mathrm{CM}}\right) \sum_{i \in \mathcal{P}_{j,k}} m_i(u_i - \widetilde{u}_i)\left(y_i^0 - y_{j,k}^{\mathrm{CM}}\right).$$

Next, we consider each sum on the right-hand side (RHS) of (2.29) separately. For the first sum, use formulae (2.8)–(2.10) to rewrite

$$\sum_{i \in \mathcal{P}_{j,k}} m_i(u_i - \widetilde{u}_i) = \sum_{i \in \mathcal{P}_{j,k}} m_i \left[u_i - \frac{\bar{w}_{j,k}^2 + (s_x^2)_{j,k}\left(x_i^0 - x_{j,k}^{\mathrm{CM}}\right) + (s_y^2)_{j,k}\left(y_i^0 - y_{j,k}^{\mathrm{CM}}\right)}{\bar{w}_{j,k}^1 + (s_x^1)_{j,k}\left(x_i^0 - x_{j,k}^{\mathrm{CM}}\right) + (s_y^1)_{j,k}\left(y_i^0 - y_{j,k}^{\mathrm{CM}}\right)} \right]$$

$$= \sum_{i \in \mathcal{P}_{j,k}} m_i \left\{ u_i - \frac{1}{\bar{w}_{j,k}^1} \left[\bar{w}_{j,k}^2 + (s_x^2)_{j,k}\left(x_i^0 - x_{j,k}^{\mathrm{CM}}\right) + (s_y^2)_{j,k}\left(y_i^0 - y_{j,k}^{\mathrm{CM}}\right) \right] \right.$$

$$(2.30) \quad \times \left. \left[1 + \frac{(s_x^1)_{j,k}\left(x_i^0 - x_{j,k}^{\mathrm{CM}}\right) + (s_y^1)_{j,k}\left(y_i^0 - y_{j,k}^{\mathrm{CM}}\right)}{\bar{w}_{j,k}^1} \right]^{-1} \right\}.$$

Taking into account (2.19), the last term in (2.30) is equal to

$$1 - \frac{(s_x^1)_{j,k}\left(x_i^0 - x_{j,k}^{\mathrm{CM}}\right) + (s_y^1)_{j,k}\left(y_i^0 - y_{j,k}^{\mathrm{CM}}\right)}{\bar{w}_{j,k}^1} + \mathcal{O}(\varepsilon^2),$$

and thus

$$\sum_{i\in\mathcal{P}_{j,k}} m_i(u_i - \widetilde{u}_i) = \frac{1}{\bar{w}_{j,k}^1}\left\{\bar{w}_{j,k}^1 \sum_{i\in\mathcal{P}_{j,k}} m_i u_i\right.$$

$$- \sum_{i\in\mathcal{P}_{j,k}} m_i\left[\bar{w}_{j,k}^2 - \frac{\bar{w}_{j,k}^2}{\bar{w}_{j,k}^1}\left((s_x^1)_{j,k}\left(x_i^0 - x_{j,k}^{\mathrm{CM}}\right) + (s_y^1)_{j,k}\left(y_i^0 - y_{j,k}^{\mathrm{CM}}\right)\right)\right.$$

$$\left.\left. + (s_x^2)_{j,k}\left(x_i^0 - x_{j,k}^{\mathrm{CM}}\right) + (s_y^2)_{j,k}\left(y_i^0 - y_{j,k}^{\mathrm{CM}}\right) + \bar{w}_{j,k}^2\mathcal{O}(\varepsilon^2)\right]\right\}.$$

Finally, using the definition of cell averages (2.8) and the fact that the center of mass $\left(x_{j,k}^{\mathrm{CM}}, y_{j,k}^{\mathrm{CM}}\right)$ satisfies (2.11), we obtain

$$\sum_{i\in\mathcal{P}_{j,k}} m_i(u_i - \widetilde{u}_i) = \frac{1}{\bar{w}_{j,k}^1}\left\{\sum_{i\in\mathcal{P}_{j,k}} m_i\left(x_i^0 - x_{j,k}^{\mathrm{CM}}\right)\left[\frac{\bar{w}_{j,k}^2}{\bar{w}_{j,k}^1}(s_x^1)_{j,k} - (s_x^2)_{j,k}\right]\right.$$

$$\left. + \sum_{i\in\mathcal{P}_{j,k}} m_i\left(y_i^0 - y_{j,k}^{\mathrm{CM}}\right)\left[\frac{\bar{w}_{j,k}^2}{\bar{w}_{j,k}^1}(s_y^1)_{j,k} - (s_y^2)_{j,k}\right] + \bar{w}_{j,k}^2\mathcal{O}(\varepsilon^2)\sum_{i\in\mathcal{P}_{j,k}} m_i\right\}$$

$$(2.31) \quad = \Delta x\Delta y\bar{w}_{j,k}^2\mathcal{O}(\varepsilon^2) = \sum_{i\in\mathcal{P}_{j,k}} m_i u_i \cdot \mathcal{O}(\varepsilon^2).$$

Remark. Note that if $(\mathbf{s}_x)_{j,k} = (\mathbf{s}_y)_{j,k} = \mathbf{0}$, then the RHS of (2.31) vanishes and $\sum_{i\in\mathcal{P}_{j,k}} m_i(u_i - \widetilde{u}_i) = 0$. Otherwise, one has an approximate x-momentum conservation only.

We next consider the second sum on the RHS of (2.29) and in a similar manner obtain

$$\sum_{i\in\mathcal{P}_{j,k}} m_i(u_i - \widetilde{u}_i)\left(x_i^0 - x_{j,k}^{\mathrm{CM}}\right) = \frac{1}{\bar{w}_{j,k}^1}\left\{\bar{w}_{j,k}^1 \sum_{i\in\mathcal{P}_{j,k}} m_i u_i\left(x_i^0 - x_{j,k}^{\mathrm{CM}}\right)\right.$$

$$- \sum_{i\in\mathcal{P}_{j,k}} m_i\left(x_i^0 - x_{j,k}^{\mathrm{CM}}\right)\left(\bar{w}_{j,k}^2 + \left[(s_x^2)_{j,k} - \frac{\bar{w}_{j,k}^2}{\bar{w}_{j,k}^1}(s_x^1)_{j,k}\right]\left(x_i^0 - x_{j,k}^{\mathrm{CM}}\right)\right.$$

$$\left.\left. + \left[(s_y^2)_{j,k} - \frac{\bar{w}_{j,k}^2}{\bar{w}_{j,k}^1}(s_y^1)_{j,k}\right]\left(y_i^0 - y_{j,k}^{\mathrm{CM}}\right) + \bar{w}_{j,k}^2\mathcal{O}(\varepsilon^2)\right)\right\}$$

$$(2.32) \quad = \sum_{i\in\mathcal{P}_{j,k}} m_i u_i\left(x_i^0 - x_{j,k}^{\mathrm{CM}}\right) + \sum_{i\in\mathcal{P}_{j,k}} m_i u_i \cdot \mathcal{O}(\varepsilon^2).$$

Then, using the definition of the center of mass (2.11) we rewrite the first term on the RHS of (2.32) as

$$\sum_{i\in\mathcal{P}_{j,k}} m_i u_i\left(x_i^0 - x_{j,k}^{\mathrm{CM}}\right) = \sum_{i\in\mathcal{P}_{j,k}} m_i u_i x_i^0 - \frac{\displaystyle\sum_{i\in\mathcal{P}_{j,k}} m_i u_i \sum_{l\in\mathcal{P}_{j,k}} m_l x_l^0}{\displaystyle\sum_{l\in\mathcal{P}_{j,k}} m_l}$$

$$= \frac{\displaystyle\sum_{i,l\in\mathcal{P}_{j,k}}\left(m_l m_i u_i x_i^0 - m_i m_l u_i x_l^0\right)}{\displaystyle\sum_{l\in\mathcal{P}_{j,k}} m_l} = \frac{\displaystyle\sum_{i,l\in\mathcal{P}_{j,k}:i<l} m_i m_l\left(x_i^0 - x_l^0\right)\left(u_i - u_l\right)}{\displaystyle\sum_{l\in\mathcal{P}_{j,k}} m_l},$$

and conclude with
(2.33)
$$\sum_{i\in\mathcal{P}_{j,k}} m_i(u_i-\widetilde{u}_i)\left(x_i^0-x_{j,k}^{\mathrm{CM}}\right) = \frac{\sum_{i,l\in\mathcal{P}_{j,k}:i<l} m_im_l\left(x_i^0-x_l^0\right)(u_i-u_l)}{\sum_{l\in\mathcal{P}_{j,k}} m_l}+\sum_{i\in\mathcal{P}_{j,k}} m_iu_i\cdot\mathcal{O}(\varepsilon^2).$$

The estimate on the third sum on the RHS of (2.29) is completely analogous:
(2.34)
$$\sum_{i\in\mathcal{P}_{j,k}} m_i(u_i-\widetilde{u}_i)\left(y_i^0-y_{j,k}^{\mathrm{CM}}\right) = \frac{\sum_{i,l\in\mathcal{P}_{j,k}:i<l} m_im_l\left(y_i^0-y_l^0\right)(u_i-u_l)}{\sum_{l\in\mathcal{P}_{j,k}} m_l}+\sum_{i\in\mathcal{P}_{j,k}} m_iu_i\cdot\mathcal{O}(\varepsilon^2).$$

We now substitute (2.31), (2.33), and (2.34) into (2.29) and sum up all $R_{j,k}^2$ to end up with the following estimate:

$$(2.35)\qquad |R^2| \le C\varepsilon\sum_{j,k}\left(\frac{\sum_{i,l\in\mathcal{P}_{j,k}:i<l} m_im_l|u_i-u_l|}{\sum_{l\in\mathcal{P}_{j,k}} m_l}+\varepsilon\sum_{i\in\mathcal{P}_{j,k}} m_i|u_i|\right).$$

• A similar estimate on R^3 is obtained from the *y-momentum conservation* equation,

$$(2.36)\qquad |R^3| \le C\varepsilon\sum_{j,k}\left(\frac{\sum_{i,l\in\mathcal{P}_{j,k}:i<l} m_im_l|v_i-v_l|}{\sum_{l\in\mathcal{P}_{j,k}} m_l}+\varepsilon\sum_{i\in\mathcal{P}_{j,k}} m_i|v_i|\right).$$

Finally, adding up (2.27), (2.35), and (2.36), and considering velocity corrections occurring in different auxiliary cells to be different events from the set E_{C2}, we obtain the estimate (2.18) in Case II.

This completes the proof of the theorem since in our 2-D sticky particle method the only contributions to the residual **R** come from the particle interactions enforced by the merger (Case I) and velocity correction (Case II) procedures. □

Remark. Note that as has been shown in the proof (see the estimate (2.31) and the remark after it), the use of the second-order reconstruction (2.10) results in additional errors in momenta conservation equations compared with the first-order $((\mathbf{s}_x)_{j,k} = (\mathbf{s}_y)_{j,k} = 0$ for all $j,k)$ approach. However, a more accurate velocity reconstruction typically leads to a more accurate particle dynamics, while the momenta conservation errors and their contributions to the corresponding residuals (the second terms on the RHS of (2.35) and (2.36)) are relatively small.

We conclude this section with a brief discussion of the result established in Theorem 2.1, which provides us with an estimate on the size of the residual. We view this result as a step toward the convergence proof of the proposed 2-D sticky particle method. Completing the proof would require obtaining more precise estimates on the residual, which, in general, may be rather difficult. However, according to the conjecture in [21], the following scenario of mass concentration occurs. Let us first mention that the system (1.5) has straight bicharacteristic lines, which usually intersect at some time moment (analogously to the 1-D case) and form curves in the (x,y)-plane (their representation in the (t,x,y)-space is not a characteristic surface, but a surface defined by a generalization of the Hugoniot relations) with a finite mass distributed

along the curves as a δ-function. These curves then start to impinge each other and form the singularities with finite masses at separate points. The collisions of the curves take place, in general, transversally, but no rigorous theoretical description of such a solution behavior is available. Assuming now that solutions of (1.5) have such a structure (this assumption has also been supported by the numerical experiments reported in section 3.2, Examples 7, 8a, and 8b), it is possible to show that $|\mathbf{R}| \to 0$ as $N \to \infty$.

Indeed, following the above scenario when particles coalesce (Case I) they form curves with finite masses. In this case, the differences $|u_i - u_l|$ and $|v_i - v_l|$ are finite, the considered cluster of particles $\mathcal{P}$ merges into a particle with mass $\sim \varepsilon$, while other, nonclustered, particles have masses $\sim \varepsilon^2$. Also, $m_l \sim \varepsilon^2$ and $|\mathcal{P}| \sim 1/\varepsilon$. Thus, $\sum_{l \in \mathcal{P}} m_l \sim \varepsilon$, $\sum_{i,l \in \mathcal{P}: i<l} m_i m_l \sim \varepsilon^3$, and hence one gets $|\mathbf{R}| \sim \varepsilon^3 \cdot N_{\mathrm{C1}}$. Finally, $N_{\mathrm{C1}} < C/\varepsilon^2$ since it is bounded by the total number of particles N, and thus we obtain that $|\mathbf{R}| \sim \varepsilon$, which tends to zero as N tends to infinity.

We now consider the situation of "pure" Case 2, when only the velocities correction procedure is performed and no particles coalesce. In this case, taking into account that the corrected velocities are also close and masses of particles are of order ε^2, one has $|\mathbf{R}| \sim \varepsilon^4 \cdot N_{\mathrm{C2}}$. But, as has been mentioned before, $N_{\mathrm{C2}} \sim N^{3/2} \sim 1/\varepsilon^3$, and thus we obtain that $|\mathbf{R}| \sim \varepsilon$ in Case II as well.

We hope that the presented heuristic convergence arguments can be "upgraded" to a rigorous convergence proof and we plan to do so in forthcoming papers.

3. Numerical examples. In this section, we test the new sticky particle (SP) method presented in section 2 on a number of 1-D and 2-D numerical examples. We also compare solutions computed by the particle method with the corresponding solutions computed using the second-order semidiscrete central-upwind (CU) scheme, developed in [11, 12, 14]. A brief description of the CU scheme for the pressureless gas dynamics system (1.5) is provided in Appendix A.

Note that in all the examples below, we do not reconstruct point values of the computed density from its particle distribution at the final time but rather plot the total mass m of each particle. For the purpose of fair comparison, the solutions computed by the finite-volume CU scheme are always presented in a similar way, that is, we plot the total mass in each cell rather than the corresponding cell averages.

3.1. One-dimensional examples. The following four examples are devoted to the 1-D system (1.2). A 1-D version of our SP method can be easily deduced from its 2-D formulation in section 2.

Example 1. In the first numerical test, taken from [5], we solve the system (1.2) subject to the following Riemann initial data:

$$(3.1) \qquad (\rho(x,0), u(x,0)) = \begin{cases} (1.00, \ 0.5) & \text{if } x < 0, \\ (0.25, -0.4) & \text{if } x > 0. \end{cases}$$

In this example, a δ-shock develops immediately and propagates with speed 0.2.

We take $\Delta x = 0.005$ for the CU scheme and the initial uniform distribution of particles, placed Δx away from each other, for the SP method. In Figure 1, the particle/cell masses and the corresponding velocities, computed by both the SP method and the CU scheme, are plotted at time $t = 0.5$. Note that because of the point mass concentration occurring at the δ-shock, the masses are presented in the logarithmic scale so that a more detailed structure of the solution can be seen.
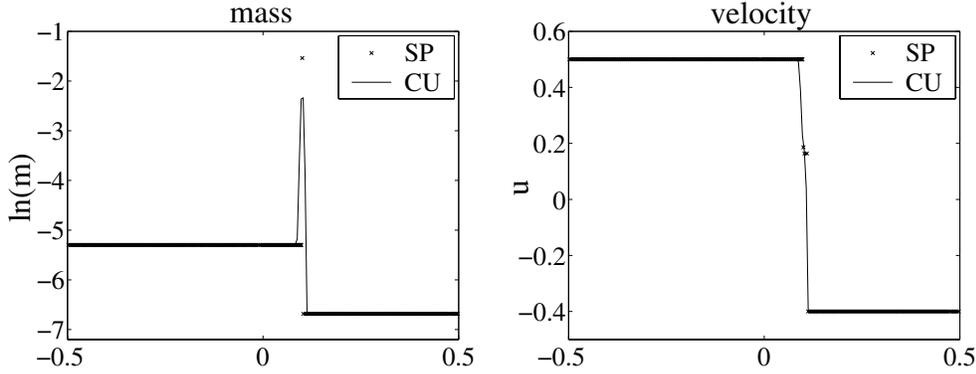
FIG. 1. *Solution of* (1.2), (3.1) *computed by the SP method and the CU scheme.*

Figure 1 demonstrates that both schemes are able to capture the δ-shock with the correct propagation speed, but one can clearly see the superiority of the results obtained by the SP method, which does not smear the δ-shock.

Example 2. We consider a test problem of the collision of two compactly supported clouds. The initial data, prescribed at $t = -1$, are taken from [17],

$$(3.2) \qquad (\rho(x,-1), u(x,-1)) = \begin{cases} (2, \ 1) & \text{if} \quad -2 < x < -1, \\ (1, -1) & \text{if} \quad 1 < x < 5, \\ (0, \ 0) & \text{otherwise.} \end{cases}$$

The two clouds collide at time $t = 0$. The left cloud is fully accelerated into the δ-wave at about $t \approx 1.21$ and the right cloud is fully accelerated at about $t \approx 4.25$. We use a uniform spatial grid with $\Delta x = 0.0125$ for the CU scheme. The SP method is started with 400 particles, placed only in the intervals $[-2, -1]$ and $[1, 5]$, where the dust is initially present. Figures 2 and 3 show the particle/cell masses (in the logarithmic scale) at times $t = -1$, -0.5, 0, 0.5, 1, 1.5, 3.5, and 6. As one can observe, both methods give the same correct location of the δ-wave. However, both the δ-wave and the contact discontinuities computed by the CU scheme are smeared over a number of cells, while the resolution achieved by the SP method is almost perfect. We note that the mass computed by the SP method is concentrated in a single point by time $t = 6$.

Example 3. In this example, we demonstrate an interaction of two singular shocks by numerically solving the system (1.2) subject to the following initial data:

$$(3.3) \qquad (\rho(x,0), u(x,0)) = \begin{cases} (0.25, 1.00) & \text{if} \ -2.75 < x < -0.75, \\ (0.25, 0.50) & \text{if} \ -0.75 < x < 0.5, \\ (1.00, -1.00) & \text{if} \quad 0.5 < x < 1.5, \\ (0.00, 0.00) & \text{otherwise.} \end{cases}$$

In Figure 4, we plot the particle/cell masses (in the logarithmic scale) computed by both the SP method and the CU scheme at times $t = 0$, 0.5, 1, 1.5, 2, and 2.5. We start the SP method with $N = 425$ particles, which are uniformly distributed in the interval $[-2.75, 1.5]$. For the CU scheme, we use a uniform spatial grid with $\Delta x = 0.01$. Again, one can clearly see that the SP method outperforms the finite-volume CU scheme by far.
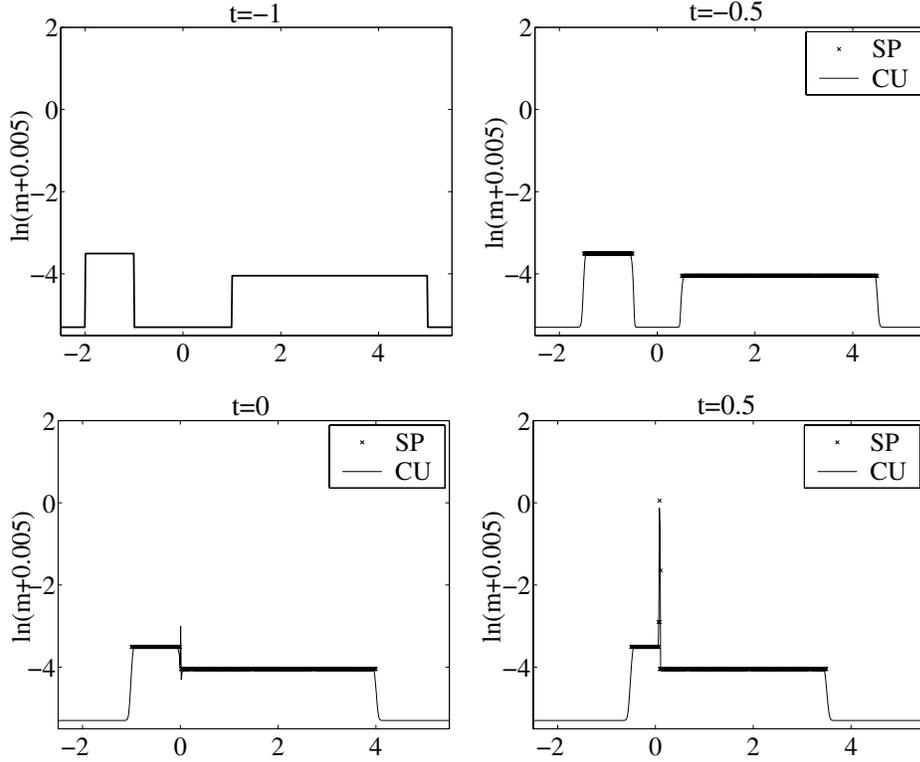
FIG. 2. *Solution (masses) of* (1.2), (3.2) *computed by the SP method and the CU scheme.*

Example 4. The last 1-D example is devoted to a problem where the velocity u changes its sign in the region with varying density. This significantly increases the level of complexity of the problem due to a special way the singularity forms, as demonstrated below.

We consider the system (1.2) subject to the smooth initial data:

(3.4)
$$\rho(x,0) = \begin{cases} 2 - \sin x & \text{if } -\pi \le x \le \pi, \\ 0 & \text{otherwise,} \end{cases} \qquad u(x,0) = \begin{cases} 1 - x & \text{if } -\pi \le x \le \pi, \\ 0 & \text{otherwise,} \end{cases}$$

for which the exact solution can be found analytically as follows. A continuous part of the solution is obtained by the method of characteristics:

(3.5)
$$u(X(t),t) = 1 - x_0, \qquad \rho(X(t),t) = \frac{2 - \sin x_0}{1 - t},$$

where

(3.6)
$$X(t) = x_0 + t(1 - x_0)$$

is the characteristic line starting at $x = x_0$. Obviously, the solution (3.5)–(3.6) is valid in the domain bounded by the characteristics $X_-(t) = -\pi + t(1 + \pi)$ and $X_+(t) = \pi + t(1 - \pi)$ and thus exists until $t = 1$ only; see Figure 5.

As t approaches 1, the density tends to infinity, more and more mass is concentrated near the point $x = 1$, and therefore one can anticipate a massive particle
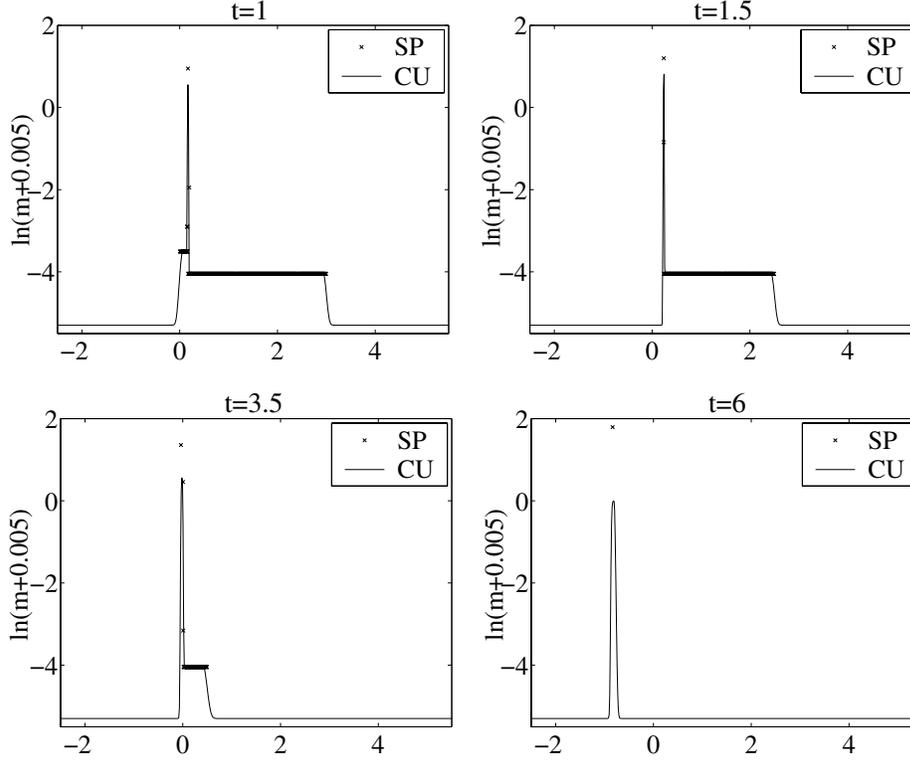
FIG. 3. *Solution (masses) of* (1.2), (3.2) *computed by the SP method and the CU scheme.*

formation at this point. In order to determine a singular part of the solution of (1.2), (3.4) we use the variational representation of the generalized solution of pressureless gas dynamics equations introduced in [8]. To this end, we consider the function

$$(3.7) \qquad F(x_0) \equiv F(x_0; x, t) := \int_0^{x_0} [s - x + t\, u(s, 0)]\, \rho(s, 0)\, ds$$

$$= \int_0^{x_0} [s - x + t\,(1 - s)]\,(2 - \sin s)\, ds,$$

and according to [8], the smoothness of the solution depends on a number of points at which the global minimum of F is attained. If F has only one global minimum point, then the solution is continuous at (x, t); otherwise the solution develops a shock discontinuity in velocity and a δ-shock in density there. In the latter case, suppose that there exists a set of points $\{x_0^1, x_0^2, \ldots\}$ at which F assumes its global minimum and denote $x_0^- := \min\{x_0^1, x_0^2, \ldots\}$ and $x_0^+ := \max\{x_0^1, x_0^2, \ldots\}$. Then the left and right values of ρ and u at (x, t) are computed from (3.5) with $x_0 = x_0^-$ and $x_0 = x_0^+$, respectively. In addition, the δ-function singularity at this point ("a massive particle") has the following mass and momentum:

$$(3.8) \qquad M = \int_{x_0^-}^{x_0^+} \rho(s, 0)\, ds, \qquad I = \int_{x_0^-}^{x_0^+} u(s, 0)\rho(s, 0)\, ds,$$

and according to mass and momentum conservation, the speed of the massive particle
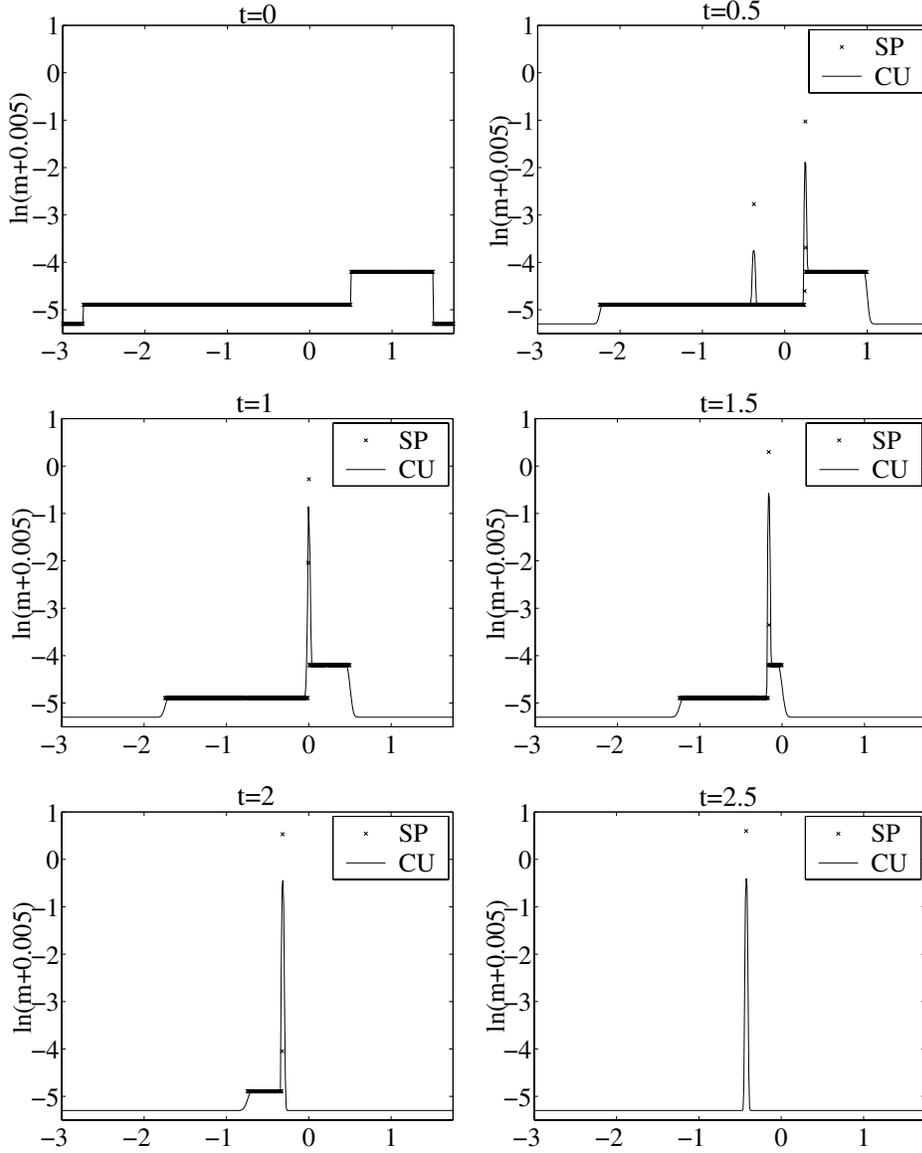
FIG. 4. *Solution (masses) of* (1.2), (3.3) *computed by the SP method and the CU scheme.*

is

$$(3.9) \qquad \frac{dX}{dt} = \frac{I}{M}.$$

For the problem under consideration, the singularity is first formed at the point $(x,t) = (1,1)$, and for $t \geq 1$, the global minimum of F is attained at two points only: $x_0^- = -\pi$ and $x_0^+ = \pi$. Therefore, by $t = 1$ all the mass is concentrated in one massive particle with the mass $M = 4\pi$ and the momentum $I = 6\pi$ (according to (3.8)), and the movement of this particle is described, according to (3.9), by the formula $X(t) = (3t - 1)/2$, $t \geq 1$; see Figure 5.
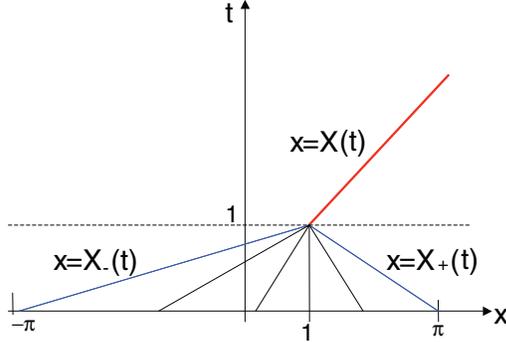
FIG. 5. *Characteristics diagram for the initial-value problem* (1.2), (3.4).
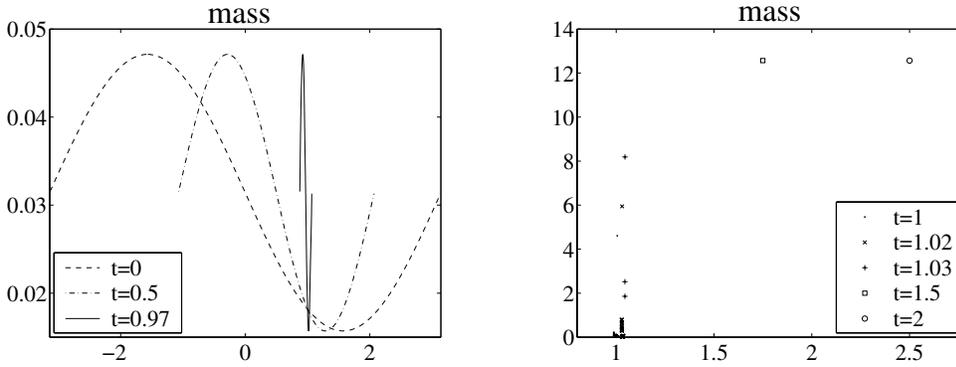
FIG. 6. *Solution (masses) of* (1.2), (3.4) *computed by the SP method for $t < 1$ (left), when the solution is smooth inside its shrinking support, and for $t \geq 1$ (right), when the total mass $M = 4\pi$ is concentrated in one particle, propagating with the constant speed $I/M = 3/2$. Note that due to a certain arbitrariness in the selection of the unification parameter d_{cr}, the final collapse of the numerical solution occurs at a slightly later time $t \approx 1.03$.*

We now turn to the presentation of our numerical results. We start the SP simulations with 400 particles uniformly distributed over the interval $[-\pi, \pi]$. In Figure 6, we plot the particle masses computed by the SP method only, since the CU scheme could not be applied to this problem at large times ($t \sim 1$ and larger). We note that, as indicated in [17], other finite-volume methods are likely to fail to capture the solution of the initial-value problem (1.2), (3.4) as well.

3.2. Two-dimensional examples.

Example 5. We start by numerically solving the 2-D analogue of the 1-D problem considered in Example 1, namely, we solve the system (1.5) in the square domain $[-1, 1] \times [-1, 1]$ subject to the 1-D Riemann initial data, artificially extended to two space dimensions:

$$(3.10) \qquad (\rho(x,y,0), u(x,y,0), v(x,y,0)) = \begin{cases} (1.00, \ 0.5, \ 0) & \text{if } x < 0, \\ (0.25, -0.4, \ 0) & \text{if } x > 0. \end{cases}$$

The purpose of this simple example is to demonstrate the failure of the "standard" velocity recovery procedure (2.7) and the ability of the alternative procedure (2.9), developed in section 2.1, to force the desired interaction of nearby particles.

Recall that in this example a δ-shock develops immediately at the line $x = 0$ and then propagates to the right with speed 0.2. As has been already mentioned, the probability of collision of two particles approaching the same singularity curve in two dimensions is, in general, zero, and therefore using formula (2.7) for computing velocities requires a special symmetric setting of the initial locations of particles; see Figure 7 (left). Obviously, if at time $t = 0$ the particles are placed as shown in Figure 7 (right) and if the unification parameter is reasonably small ($d_{cr} < \Delta y/2$), the particles moving from the left and from the right will never interact and the δ-shock will not be captured numerically. We note that for a more complicated, truly 2-D initial data it may be impossible to impose any kind of symmetry, so the situation with the data as in Figure 7 (right) is generic.
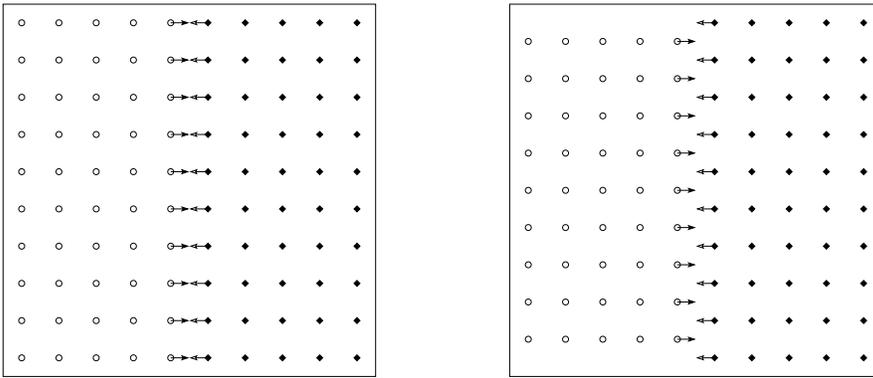
FIG. 7. *Initial locations of particles in Example* 5: *symmetric (left) and asymmetric (right) cases.*

On the other hand, the velocity recovery procedure (2.9) ensures an interaction between particles independently of their initial placement. In Figures 8 and 9, we show the masses and x-velocities of the particles at time $t = 0.5$. They are computed by the SP method with the initial locations of particles as in Figure 7 (left) and Figure 7 (right), respectively. As one can see, in both cases the SP method combined with the velocity recovery procedure (2.9) leads to the desired clustering of particles at the singularity. Moreover, the resolution achieved in the case of asymmetric initial particle distribution is almost as good as in the symmetric case.

Example 6. Next, we turn to genuinely 2-D problems. First, consider the system (1.5) subject to the following initial data:

$$(3.11) \qquad (\rho(x,y,0), u(x,y,0), v(x,y,0)) = \begin{cases} (2,2,1) & \text{if } (x,y) \in \Omega, \\ (0,0,0) & \text{if } (x,y) \in \partial\Omega, \\ (1,0,0) & \text{otherwise}, \end{cases}$$

where $\Omega = \{x < 0,\, y < 1\} \cup \{x > 0,\, y > 0,\, x^2 + y^2 < 1\} \cup \{y < 0,\, 0 < x < 1\}$. The initial location of the discontinuity $\partial\Omega$ is shown in Figure 10. According to [21], the exact solution of the initial-value problem (1.5), (3.11) develops a δ-shock in density,
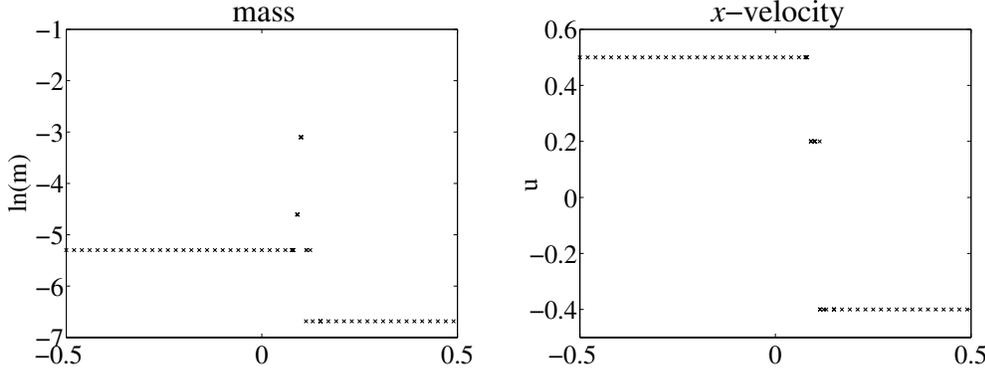
FIG. 8. *Side view on the solution of* (1.5), (3.10) *computed by the SP method. The initial location of particles is shown in Figure* 7 *(left).*
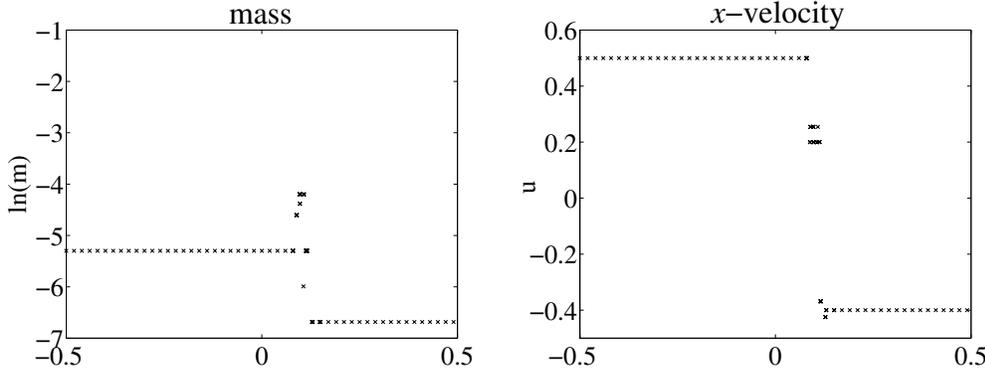

FIG. 9. *Side view on the solution of* (1.5), (3.10) *computed by the SP method. The initial location of particles is shown in Figure* 7 *(right).*

and the evolution of the shock curve is described by the following system of ODEs:

$$(3.12) \quad \begin{cases} \dfrac{dX}{dt} = u_- \dfrac{\sqrt{\rho_-}}{\sqrt{\rho_-} + \sqrt{\rho_+}} = \dfrac{2\sqrt{2}}{\sqrt{2}+1}, \\[3mm] \dfrac{dY}{dt} = v_- \dfrac{\sqrt{\rho_-}}{\sqrt{\rho_-} + \sqrt{\rho_+}} = \dfrac{\sqrt{2}}{\sqrt{2}+1}, \end{cases}$$

where $(\rho_-, u_-, v_-) := (2, 2, 1)$ are the initial values inside the domain Ω and $\rho_+ := 1$ is the initial value of the density on the other side of the initial shock curve.

Numerically, we restrict the initial data (3.11) to the finite domain $[-4, 4] \times [-4, 4]$ and consider the following initial-boundary value problem: (1.5), (3.11) together with the solid wall boundary conditions. The numerical solutions, computed by the SP method at time $t = 2$ with 50×50 and 100×100 initially uniformly distributed particles, are plotted in Figure 10. The size of each point in the figure is proportional to the mass accumulated in the particle located there. The exact solution of the initial-boundary value problem is not known, but in the domain $[0, 4] \times [-2, 4]$ it coincides with the solution of the original initial-value problem (1.5), (3.11), and as can be clearly seen in Figure 10, the SP method accurately tracks the evolution of
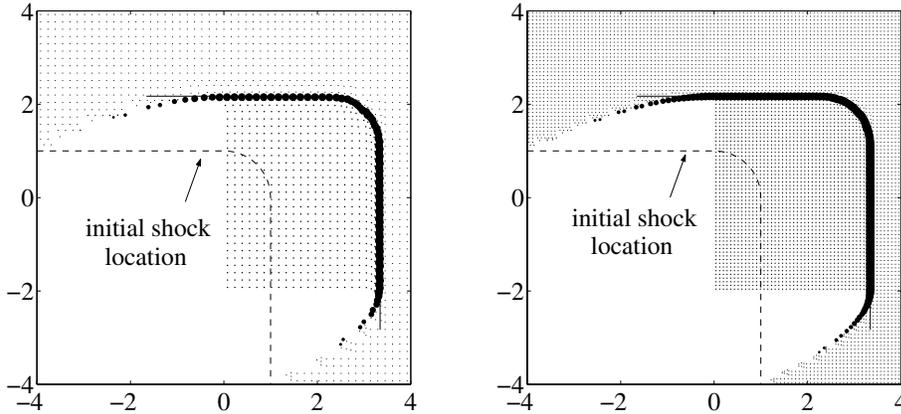
FIG. 10. *Top view on the solution (masses) of* (1.5), (3.11) *computed by the SP method with* 50×50 *(left) and* 100×100 *(right) particles. The solid line is obtained from the initial shock curve (the dashed line) by the evolution according to* (3.12).

the corresponding part of the shock curve described by (3.12). Outside the domain $[0, 4] \times [-2, 4]$, the solution is obviously affected by the boundedness of the cloud, but the obtained numerical solution looks reasonable, as supported by the performed mesh refinement study.

Example 7. Next, we consider an example with nonzero mass and momenta at the initial shock curve. We numerically solve the system (1.5) subject to the following initial data:

$$(3.13) \qquad (\rho(\mathbf{x}, 0), u(\mathbf{x}, 0), v(\mathbf{x}, 0)) = \begin{cases} (2, 2, 2) & \text{if } \mathbf{x} \in \Omega, \\ (10\,\delta(\mathrm{dist}(\mathbf{x}, \partial\Omega)), 2, 1) & \text{if } \mathbf{x} \in \partial\Omega, \\ (2, 0, 0) & \text{otherwise,} \end{cases}$$

where $\mathbf{x} \equiv (x, y)$ and the domain Ω is the same as in Example 6: $\Omega = \{x < 0, y < 1\} \cup \{x > 0, y > 0, x^2 + y^2 < 1\} \cup \{y < 0, 0 < x < 1\}$. In the practical implementation, we replace the δ-function along the curve $\partial\Omega$ with its approximation by a step function; namely, we take

$$\rho(\mathbf{x}, 0) = \begin{cases} \dfrac{10\sqrt{2}}{\sqrt{(\Delta x)^2 + (\Delta y)^2}} & \text{if } \mathrm{dist}(\mathbf{x}, \partial\Omega) \leq \dfrac{\sqrt{(\Delta x)^2 + (\Delta y)^2}}{2\sqrt{2}} \\ 2, & \text{otherwise.} \end{cases}$$

The numerical solutions at time $t = 1.5$ obtained using the SP method with 101×101 particles (initially uniformly distributed) and the CU scheme with $\Delta x = \Delta y = 0.08$ are plotted in Figures 11 and 12. Note that the maximal mass value of the solution obtained by the CU scheme is 0.6299 while the maximal mass obtained by the SP method is 2.7009. As before, the size of each point in the figures is proportional to the mass accumulated in the particle located there.

Even though a complete structure of the exact solution of the initial-value problem (1.5), (3.13) is not available, the obtained solution behavior has been expected (see the discussion at the end of section 2). It is instructive to compare the computed numerical solution with theoretical results presented in [21]. According to [21], if
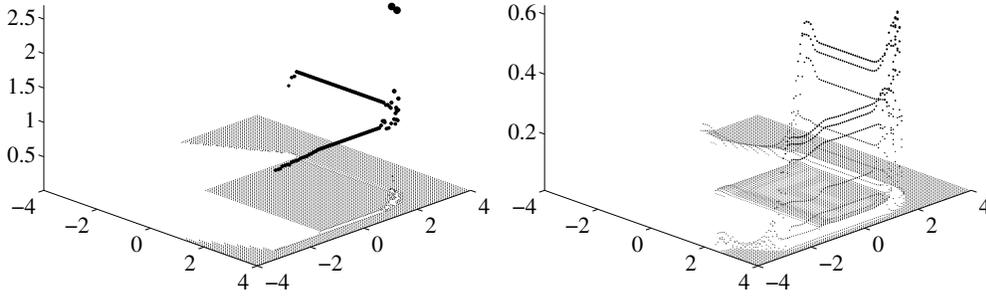
FIG. 11. *Solution (masses) of* (1.5), (3.13) *computed by the SP method (left) and the CU scheme (right).*
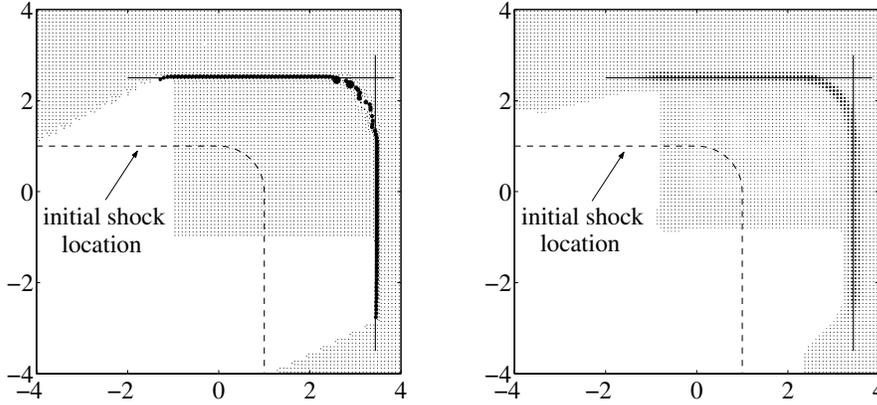

FIG. 12. *Top view on the solution (masses) of* (1.5), (3.13) *computed by the SP method (left) and the CU scheme (right). The solid lines are obtained from the initial shock curve (the dashed line) by the evolution according to* (3.14).

initially a shock curve with mass distribution P_0 and velocities (U_0, V_0) is located along the line $x_0(l) = C \equiv$ const, $y_0(l) = l$, then its location at a later time is given by

$$(3.14) \quad \begin{cases} x = C + \left[\dfrac{u}{2} - \dfrac{\left(\frac{1}{2}u - U_0\right) P_0}{\rho u t + P_0} \right] t, \\[4mm] uy - vx = \dfrac{(uV_0 - vU_0)P_0}{\rho u} \ln\left(1 + \dfrac{\rho u t}{P_0}\right) + ul - vC, \end{cases}$$

where ρ, u, and v are the density and the corresponding velocities inside the domain. If we now consider a part of the initial shock curve $\partial\Omega$, namely, $x_0 = 1$, $y_0 = l$, $0 \le l \le 1$, and substitute the corresponding values of $P_0 = 10$, $U_0 = 2$, $V_0 = 1$, and $\rho = u = v = 2$ into the first formula in (3.14), we obtain that at time $t = 1.5$ the shock line should be located at $x = 3.4375$. Similarly, it can be shown that the initial shock line $x_0 = l$, $y_0 = 1$, $0 \le l \le 1$ should move to $y = 2.5$ by the time $t = 1.5$. As one can see from Figure 12, both methods accurately track the evolution of the corresponding

parts of the shock curve: in this figure, the horizontal solid line ($y = 2.5$) and the vertical solid line ($x = 3.4375$) represent the exact shock locations, while the dots are used to plot the numerical solution obtained by the SP method (left) and the CU scheme (right). One can clearly observe a much better resolution of the discontinuity achieved by the SP method.

Example 8. We now consider the system (1.5) subject to the following initial data:

$$(3.15) \qquad (\rho(\mathbf{x}, 0), u(\mathbf{x}, 0), v(\mathbf{x}, 0)) = \begin{cases} (2, 2, 1) & \text{if } \mathbf{x} \in \Omega_1, \\ (2, 1, 2) & \text{if } \mathbf{x} \in \Omega_2, \\ (2, \eta, \eta) & \text{if } \mathbf{x} \in \Omega_3, \\ (0, 0, 0) & \text{if } \mathbf{x} \in \partial\Omega_1 \cup \partial\Omega_2 \cup \partial\Omega_3, \\ (1, 0, 0) & \text{otherwise,} \end{cases}$$

where $\Omega_1 = \{x < 0, \, x/2 + 1 < y < 1\}$, $\Omega_2 = \{y < 0, \, y/2 + 1 < x < 1\}$, and $\Omega_3 = \{x < 0, \, y < x/2 + 1\} \cup \{x > 0, \, y > 0, \, x^2 + y^2 < 1\} \cup \{y < 0, \, x < y/2 + 1\}$. The initial locations of the discontinuities are shown in Figures 13 and 16. As in the previous two examples, we restrict the initial data (3.15) to the finite domain $[-4, 4] \times [-4, 4]$ and supplement the initial-value problem (1.5), (3.15) with the solid wall boundary conditions.

Example 8a. We first take $\eta = 1$ in (3.15). In this case, δ-shocks are immediately formed along the initial shock curves. Then, they propagate and develop stronger δ-type singularities at two points, which later merge into a single one in the upper right corner of the computational domain (as in the previous numerical example, the exact solution of the initial-value problem (1.5), (3.15) is not available, but the obtained solution behavior is in line with our expectations; see the discussion at the end of section 2).

We apply the SP method with initially uniformly distributed 100×100 particles and present the solutions, computed at times $t = 2$ and $t = 4$, in Figures 13 and 14. Once again, the size of each point in the figures is proportional to the mass accumulated in the particle located there. For comparison purposes, we also apply the CU scheme with $\Delta x = \Delta y = 0.08$ to the same initial-boundary value problem. The obtained solution, presented in Figure 15 (left), clearly demonstrates that the resolution achieved by the SP method is by far superior. However, since the exact solution of this test problem is unavailable and since there is a very big discrepancy between the solutions computed by the SP and CU methods, we also apply the CU scheme on a much finer grid with $\Delta x = \Delta y = 0.02$. The obtained solution, shown in Figure 15 (right), looks more like the SP solution in Figure 14 (right), but the resolution is still not as high as the one achieved by our SP method; compare, for instance, the maximal mass values—7.2927, 3.9223, and 1.0205—of the solutions, computed by the SP method, the CU scheme on the fine grid, and the CU scheme on the coarse grid, respectively.

Example 8b. Next, we take $\eta = 2 - 1/\sqrt{2}$ in (3.15). In this case, we observe a more clear structure of the formed δ-shocks, which then interact with two contact waves. This interaction, as in Example 8a, leads to formation of strong singularities. Such a structure—strong singularities emerging from δ-shock curves—is anticipated as a typical one for 2-D pressureless gases; see the discussion at the end of section 2. See also [21] and the references therein.
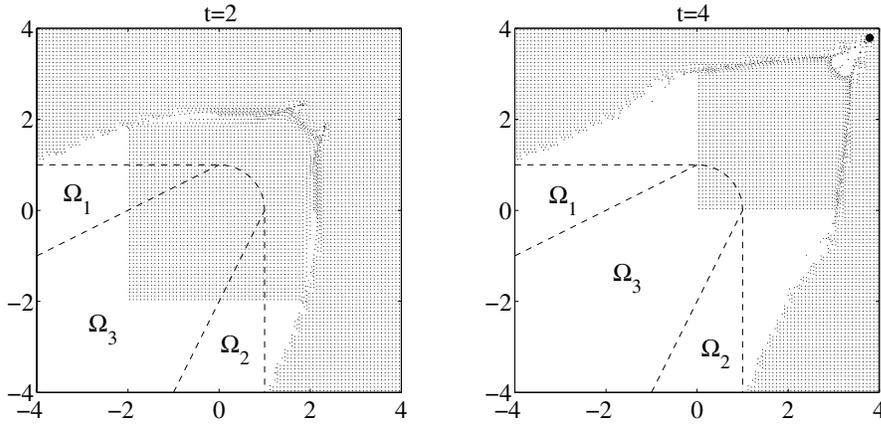
FIG. 13. *Top view on the solution (masses) of* (1.5), (3.15) *with* $\eta = 1$ *at* $t = 2$ *(left) and* $t = 4$ *(right) computed by the SP method. The dashed lines represent the initial location of discontinuities.*
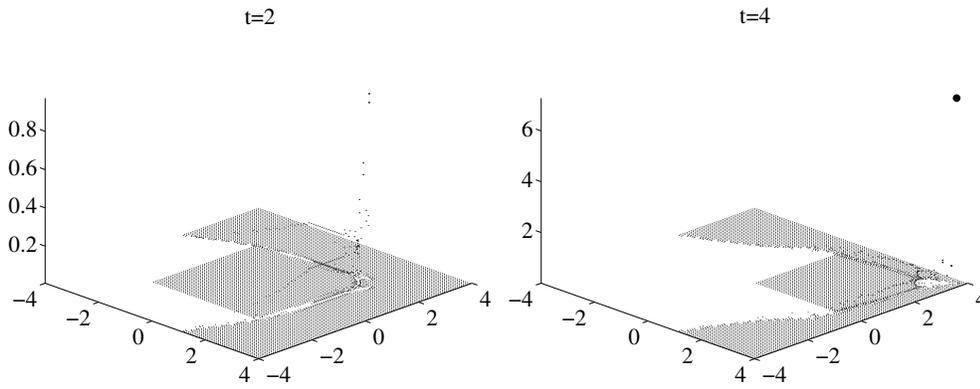

FIG. 14. *Solution (masses) of* (1.5), (3.15) *with* $\eta = 1$ *at* $t = 2$ *(left) and* $t = 4$ *(right) computed by the SP method.*
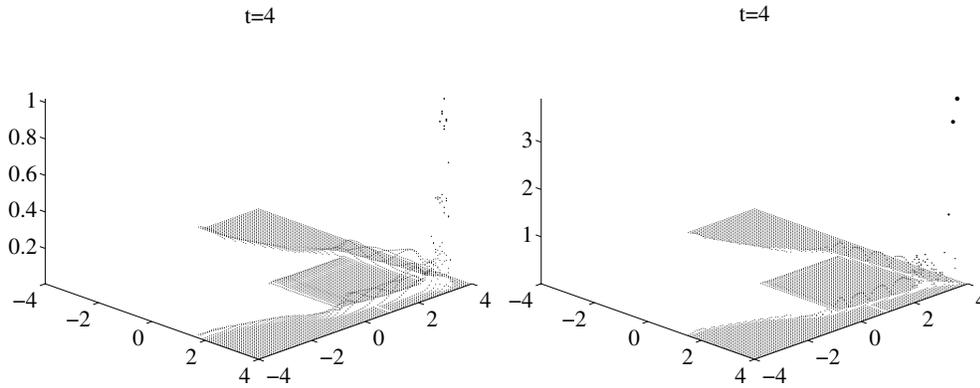
FIG. 15. *Solution (masses) of* (1.5), (3.15) *with* $\eta = 1$ *at* $t = 4$ *computed by the CU scheme with* $\Delta x = \Delta y = 0.08$ *(left) and* $\Delta x = \Delta y = 0.02$ *(right).*
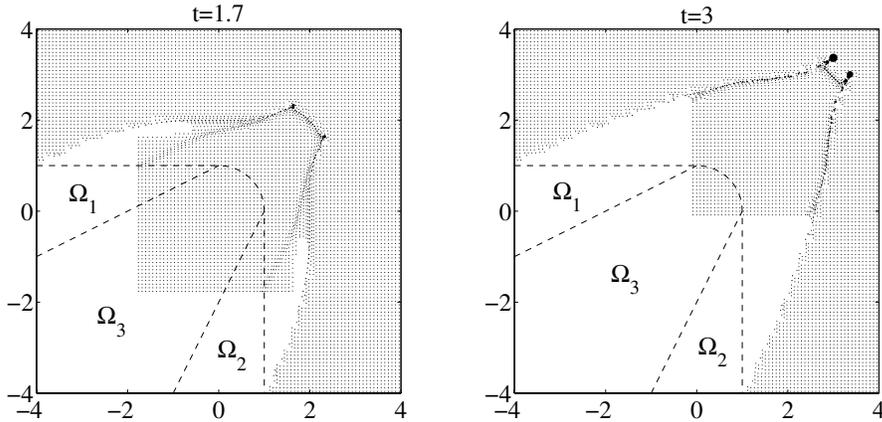
FIG. 16. *Top view on the solution (masses) of (1.5), (3.15) with $\eta = 2 - 1/\sqrt{2}$ at $t = 1.7$ (left) and $t = 3$ (right) computed by the SP method. The dashed lines represent the initial shock location.*
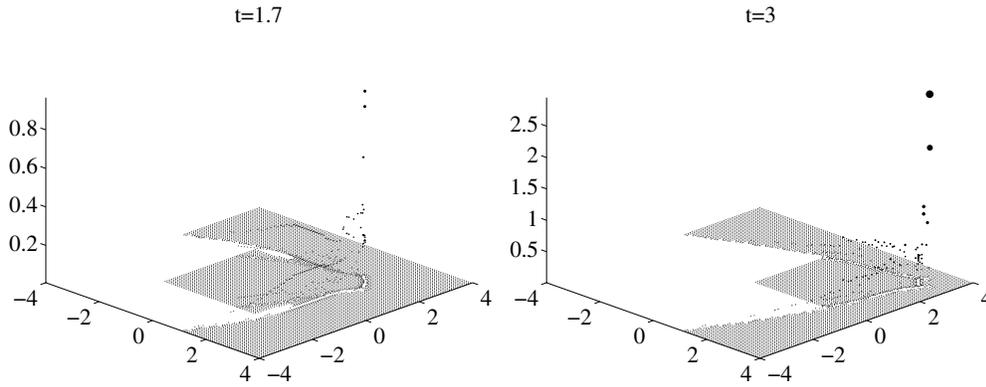

FIG. 17. *Solution (masses) of (1.5), (3.15) with $\eta = 2 - 1/\sqrt{2}$ at $t = 1.7$ (left) and $t = 3$ (right) computed by the SP method.*

We apply the SP method with initially uniformly distributed 100×100 particles and present the solutions, computed at times $t = 1.7$ and $t = 3$, in Figures 16 and 17. As before, the size of each point in these figures is proportional to the mass accumulated in the particle located there. We compare the SP solution, presented in Figure 17 (right), with the solution computed by the CU scheme with $\Delta x = \Delta y = 0.08$, which is plotted in Figure 18 (left). One can clearly see the superiority of the results achieved by the SP method. We also apply the CU scheme on a much finer grid with $\Delta x = \Delta y = 0.02$. The obtained solution, shown in Figure 18 (right), looks more like the SP solution in Figure 17 (right), but the resolution is still not as high as the one achieved by the SP method; compare, as before, the maximal mass values— 2.9529, 1.7261, and 0.4724—of the solutions, computed by the SP method, the CU scheme on the fine grid, and the CU scheme on the coarse grid, respectively.

Example 9. Finally, we consider the system (1.5) subject to the initial data taken from [1, 23]. In this example, $\rho(x, 0)$ is a Gaussian field, shown in Figures 19 and 20 (a detailed description of its generation can be found in [23, section 5.1]) and
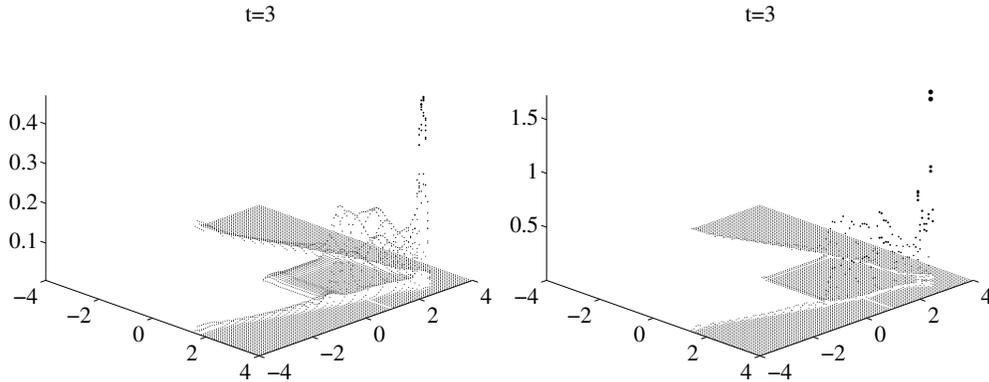
FIG. 18. *Solution (masses) of* (1.5), (3.15) *with* $\eta = 2 - 1/\sqrt{2}$ *at* $t = 3$ *computed by the CU scheme with* $\Delta x = \Delta y = 0.08$ *(left) and* $\Delta x = \Delta y = 0.02$ *(right).*

the initial velocity vector is the solution of the following elliptic problem:

(3.16)
$$\begin{cases} u = -\phi_x, \\ v = -\phi_y, \\ \Delta\phi = 4\pi G(\rho - \bar{\rho}) & \text{in } \Omega = [0, 251] \times [0, 251], \end{cases}$$

where G is the gravitational constant and $\bar{\rho} = \frac{1}{|\Omega|} \int_{\Omega} \rho \, dx \, dy$. All the boundary conditions are assumed to be periodic. Those 2-D physical data are derived from large-scale structure simulations related to the cosmological model of Zeldovich [24]. In Figures 19 and 20, we observe the formation of the large-scale structures computed by the SP method and the CU scheme, respectively. We use a uniform spatial grid with $\Delta x = \Delta y = 1$ for the CU scheme and the uniform initial distribution of 251×251 particles. In order to compare the results, the total mass of each cell computed by the CU scheme has been recalculated at the location of particles. Again, the size of each point in Figures 19 and 20 is proportional to the total mass at this point, that is, bigger points correspond to larger masses. As one can see, for small times both schemes produce very similar results, while for larger times a numerical diffusion present in the CU scheme "takes over" (compare the corresponding results at times $t = 4000$ and $t = 15000$ in Figures 19 and 20). In fact, the maximum mass accumulated at one point by the SP method is about 15 times larger than the one accumulated by the CU scheme. We also would like to point out that, as a result of unification of clustering particles, the number of particles is decreasing in time and therefore the efficiency of the SP method is increasing. For instance, the number of particles at times $t = 1000$, 4000, and 15000 is 2767, 1068, and 454, respectively, while computations using the CU scheme are being performed on 251×251 grid for all times. This also results in much smaller runtime for the SP method compared to the CU scheme.

4. Concluding remarks. We have presented a new sticky particle (SP) method for the system of Euler equations of pressureless gas dynamics that arises in the modeling of the formation of large-scale structures in the universe. The main feature of interest in this problem is the formation of strong singularities (δ-functions along the surfaces as well as at separate points) and the emergence of vacuum states, and therefore particle methods seem to be a natural choice for numerical simulations of such models. The proposed SP method has been studied both analytically and numerically.
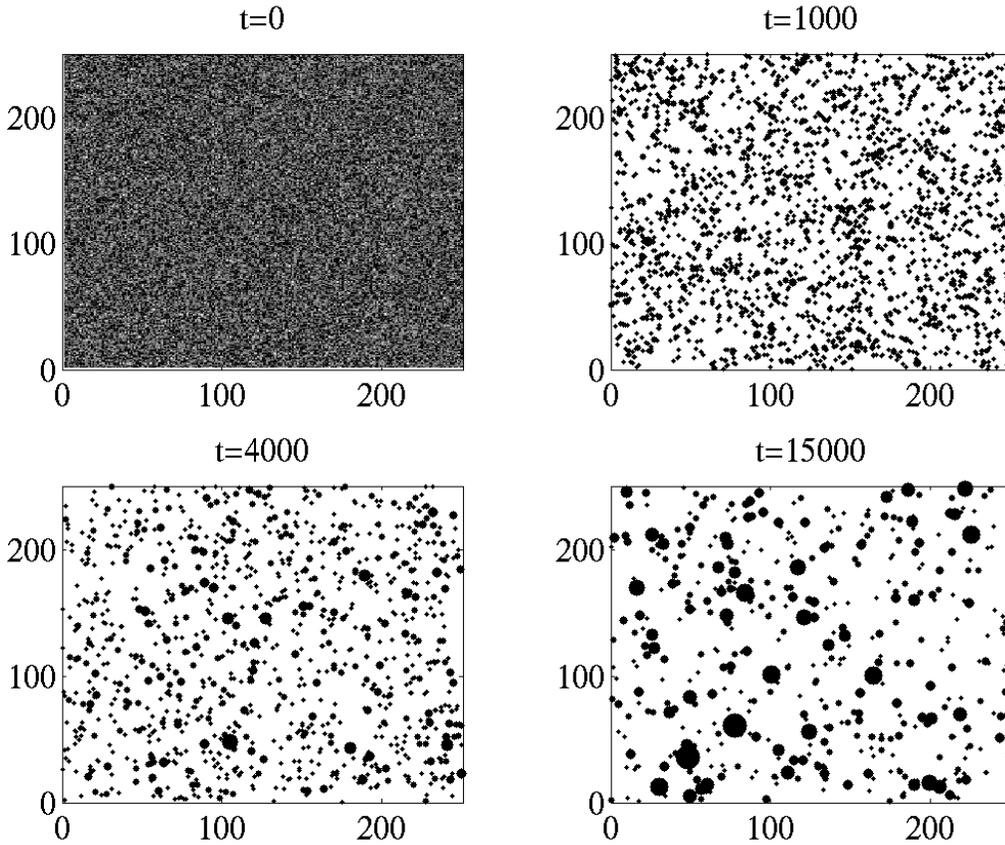
FIG. 19. *Top view on the solution (masses) of* (1.5), (3.16) *computed by the SP method at different times.*

It has been shown that the particle approximation satisfies the original system of pressureless gas dynamics in a weak sense, but only within a certain residual, which has been rigorously estimated. It has also been explained why the relevant errors should diminish as the total number of particles increases. Numerical experiments in one and two space dimensions have been performed (3-D extension of the SP method is out of scope of this paper, but it can be carried out rather straightforwardly). The SP method has been compared to the second-order CU scheme. Our numerical experiments clearly demonstrate the superiority of results obtained by the SP method, which seems to be a robust, accurate, and efficient alternative to existing numerical methods for pressureless gas dynamics.

Appendix A. Semidiscrete central-upwind schemes for pressureless gas dynamics. Here, we briefly describe semidiscrete CU schemes for the 2-D system of pressureless gas dynamics (1.5), which can be written in the following flux-vector form:

$$\mathbf{w}_t + \mathbf{f}(\mathbf{w})_x + \mathbf{g}(\mathbf{w})_y = 0,$$
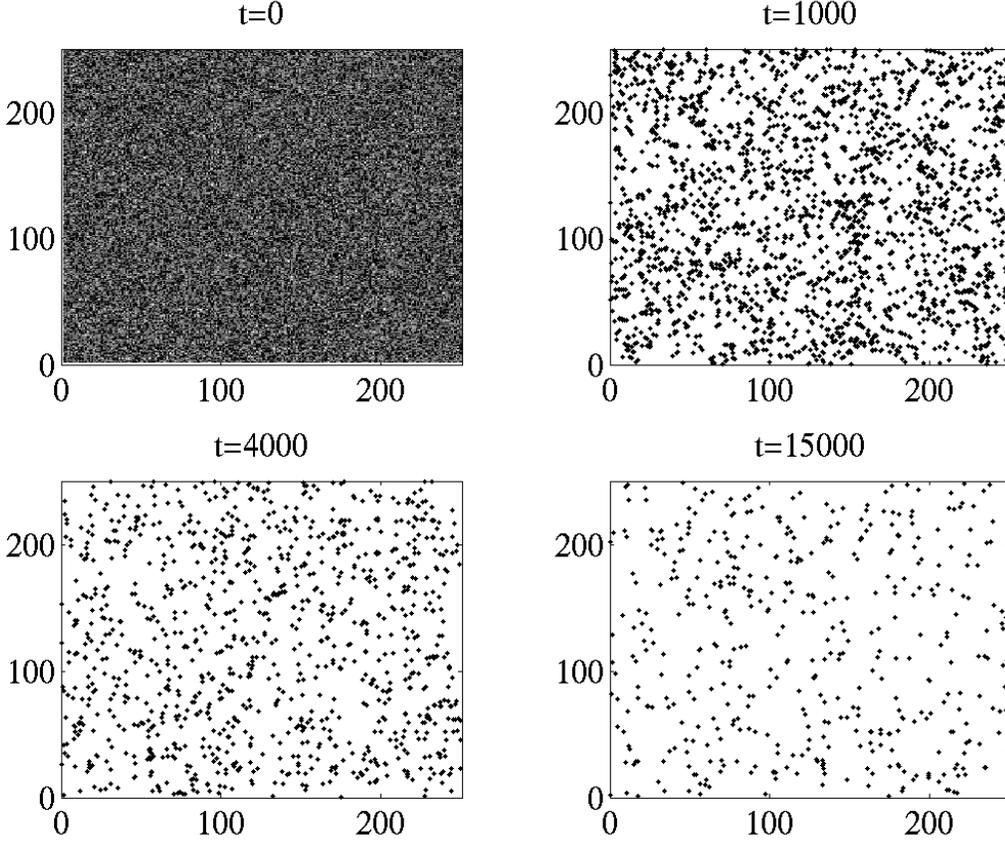
FIG. 20. *Top view on the solution (masses) of* (1.5), (3.16) *computed by the CU scheme at different times.*

where

$$\mathbf{w} := \begin{pmatrix} \rho \\ \rho u \\ \rho v \end{pmatrix}, \quad \mathbf{f}(\mathbf{w}) := \begin{pmatrix} \rho u \\ \rho u^2 \\ \rho uv \end{pmatrix}, \quad \mathbf{g}(\mathbf{w}) := \begin{pmatrix} \rho v \\ \rho uv \\ \rho v^2 \end{pmatrix}.$$

We consider a uniform spatial grid $x_\mu := \mu \Delta x$, $y_\nu := \nu \Delta y$, and denote the computed quantities, the cell averages, by

$$\bar{\mathbf{w}}_{j,k}(t) := \frac{1}{\Delta x \Delta y} \iint\limits_{I_{j,k}} \mathbf{w}(\xi, \eta, t) \, d\eta \, d\xi, \quad I_{j,k} := [x_{j-\frac{1}{2}}, x_{j+\frac{1}{2}}] \times [y_{k-\frac{1}{2}}, y_{k+\frac{1}{2}}].$$

The cell averages are evolved in time according to the semidiscrete CU scheme

$$\frac{d}{dt} \bar{\mathbf{w}}_{j,k}(t) = -\frac{H^x_{j+\frac{1}{2},k}(t) - H^x_{j-\frac{1}{2},k}(t)}{\Delta x} - \frac{H^y_{j,k+\frac{1}{2}}(t) - H^y_{j,k-\frac{1}{2}}(t)}{\Delta y},$$

where the numerical fluxes $H^x_{j+\frac{1}{2},k}$ and $H^y_{j,k+\frac{1}{2}}$ are given by (see [11] for the derivation)
(A.1)

$$H^x_{j+\frac{1}{2},k} = \frac{a^+_{j+\frac{1}{2},k}\mathbf{f}(\mathbf{w}^E_{j,k}) - a^-_{j+\frac{1}{2},k}\mathbf{f}(\mathbf{w}^W_{j+1,k})}{a^+_{j+\frac{1}{2},k} - a^-_{j+\frac{1}{2},k}} + a^+_{j+\frac{1}{2},k}a^-_{j+\frac{1}{2},k}\left[\frac{\mathbf{w}^W_{j+1,k} - \mathbf{w}^E_{j,k}}{a^+_{j+\frac{1}{2},k} - a^-_{j+\frac{1}{2},k}} - \mathbf{q}^x_{j+\frac{1}{2},k}\right]$$

and
(A.2)

$$H^y_{j,k+\frac{1}{2}} = \frac{b^+_{j,k+\frac{1}{2}}\mathbf{g}(\mathbf{w}^N_{j,k}) - b^-_{j,k+\frac{1}{2}}\mathbf{g}(\mathbf{w}^S_{j,k+1})}{b^+_{j,k+\frac{1}{2}} - b^-_{j,k+\frac{1}{2}}} + b^+_{j,k+\frac{1}{2}}b^-_{j,k+\frac{1}{2}}\left[\frac{\mathbf{w}^S_{j,k+1} - \mathbf{w}^N_{j,k}}{b^+_{j,k+\frac{1}{2}} - b^-_{j,k+\frac{1}{2}}} - \mathbf{q}^y_{j,k+\frac{1}{2}}\right].$$

Note that all the quantities in (A.1) and (A.2) depend on t, but we will omit this dependence in order to simplify the notation.

In (A.1)–(A.2), the point values $\mathbf{w}^{E(W,S,N)}$ are to be computed from a conservative, nonoscillatory piecewise polynomial reconstruction of an appropriate order. For example, the second-order CU scheme would employ a piecewise linear reconstruction

(A.3) $\widetilde{\mathbf{w}}(x,y,t) = \bar{\mathbf{w}}_{j,k}(t) + (\mathbf{w}_x)_{j,k}(x - x_j) + (\mathbf{w}_y)_{j,k}(y - y_k)$ for $(x,y) \in I_{j,k}$,

and the corresponding point values will be

$$\mathbf{w}^{E(W)}_{j,k} := \bar{\mathbf{w}}_{j,k}(t) \pm \frac{\Delta x}{2}(\mathbf{w}_x)_{j,k}, \quad \mathbf{w}^{N(S)}_{j,k} := \bar{\mathbf{w}}_{j,k}(t) \pm \frac{\Delta y}{2}(\mathbf{w}_y)_{j,k}.$$

To ensure a nonoscillatory property of this reconstruction and thus of the second-order CU scheme, the slopes in (A.3) should be computed with the help of a nonlinear limiter. In our numerical experiments, we have used a one-parameter family of the *minmod* limiters [15, 18, 22]:

$$(\mathbf{w}_x)_{j,k} = \text{minmod}\left(\theta\frac{\bar{\mathbf{w}}_{j+1,k} - \bar{\mathbf{w}}_{j,k}}{\Delta x},\ \frac{\bar{\mathbf{w}}_{j+1,k} - \bar{\mathbf{w}}_{j-1,k}}{2\Delta x},\ \theta\frac{\bar{\mathbf{w}}_{j,k} - \bar{\mathbf{w}}_{j-1,k}}{\Delta x}\right),$$

$$(\mathbf{w}_y)_{j,k} = \text{minmod}\left(\theta\frac{\bar{\mathbf{w}}_{j,k+1} - \bar{\mathbf{w}}_{j,k}}{\Delta y},\ \frac{\bar{\mathbf{w}}_{j,k+1} - \bar{\mathbf{w}}_{j,k-1}}{2\Delta y},\ \theta\frac{\bar{\mathbf{w}}_{j,k} - \bar{\mathbf{w}}_{j,k-1}}{\Delta y}\right),$$

where $\theta \in [1,2]$, and the multivariate minmod function is defined by (2.14). Notice that larger θ's correspond to less dissipative but, in general, more oscillatory limiters (we have used $\theta = 1.5$ in all the reported numerical experiments).

Since all the eigenvalues of the Jacobians $\frac{\partial \mathbf{f}}{\partial \mathbf{w}}$ and $\frac{\partial \mathbf{g}}{\partial \mathbf{w}}$ are of multiplicity 3 and are equal to u and v, respectively, the one-sided local speeds in (A.1)–(A.2) are easy to estimate:

$$a^+_{j+\frac{1}{2},k} := \max\left\{u^W_{j+1,k}, u^E_{j,k}, 0\right\}, \quad a^-_{j+\frac{1}{2},k} := \min\left\{u^W_{j+1,k}, u^E_{j,k}, 0\right\},$$
$$b^+_{j,k+\frac{1}{2}} := \max\left\{v^S_{j,k+1}, v^N_{j,k}, 0\right\}, \quad b^-_{j,k+\frac{1}{2}} := \min\left\{v^S_{j,k+1}, v^N_{j,k}, 0\right\}.$$

Finally, $\mathbf{q}^x_{j+\frac{1}{2},k}$ and $\mathbf{q}^y_{j,k+\frac{1}{2}}$ are the "antidiffusion" terms that help to reduce numerical dissipation present at nonoscillatory central schemes [11]:

$$\mathbf{q}^x_{j+\frac{1}{2},k} = \text{minmod}\left(\frac{\mathbf{w}^{NW}_{j+1,k} - \mathbf{w}^{int}_{j+\frac{1}{2},k}}{a^+_{j+\frac{1}{2},k} - a^-_{j+\frac{1}{2},k}},\ \frac{\mathbf{w}^{int}_{j+\frac{1}{2},k} - \mathbf{w}^{NE}_{j,k}}{a^+_{j+\frac{1}{2},k} - a^-_{j+\frac{1}{2},k}},\right.$$
$$\left.\frac{\mathbf{w}^{SW}_{j+1,k} - \mathbf{w}^{int}_{j+\frac{1}{2},k}}{a^+_{j+\frac{1}{2},k} - a^-_{j+\frac{1}{2},k}},\ \frac{\mathbf{w}^{int}_{j+\frac{1}{2},k} - \mathbf{w}^{SE}_{j,k}}{a^+_{j+\frac{1}{2},k} - a^-_{j+\frac{1}{2},k}}\right),$$

$$\mathbf{q}^y_{j,k+\frac{1}{2}} = \mathrm{minmod}\left(\frac{\mathbf{w}^{\mathrm{SW}}_{j,k+1} - \mathbf{w}^{\mathrm{int}}_{j,k+\frac{1}{2}}}{b^+_{j,k+\frac{1}{2}} - b^-_{j,k+\frac{1}{2}}}, \frac{\mathbf{w}^{\mathrm{int}}_{j,k+\frac{1}{2}} - \mathbf{w}^{\mathrm{NW}}_{j,k}}{b^+_{j,k+\frac{1}{2}} - b^-_{j,k+\frac{1}{2}}}, \right.$$
$$\left. \frac{\mathbf{w}^{\mathrm{SE}}_{j,k+1} - \mathbf{w}^{\mathrm{int}}_{j,k+\frac{1}{2}}}{b^+_{j,k+\frac{1}{2}} - b^-_{j,k+\frac{1}{2}}}, \frac{\mathbf{w}^{\mathrm{int}}_{j,k+\frac{1}{2}} - \mathbf{w}^{\mathrm{NE}}_{j,k}}{b^+_{j,k+\frac{1}{2}} - b^-_{j,k+\frac{1}{2}}}\right),$$

where

$$\mathbf{w}^{\mathrm{int}}_{j+\frac{1}{2},k} = \frac{a^+_{j+\frac{1}{2},k}\mathbf{w}^{\mathrm{W}}_{j+1,k} - a^-_{j+\frac{1}{2},k}\mathbf{w}^{\mathrm{E}}_{j,k} - \left\{\mathbf{f}(\mathbf{w}^{\mathrm{W}}_{j+1,k}) - \mathbf{f}(\mathbf{w}^{\mathrm{E}}_{j,k})\right\}}{a^+_{j+\frac{1}{2},k} - a^-_{j+\frac{1}{2},k}},$$

$$\mathbf{w}^{\mathrm{int}}_{j,k+\frac{1}{2}} = \frac{b^+_{j,k+\frac{1}{2}}\mathbf{w}^{\mathrm{S}}_{j,k+1} - b^-_{j,k+\frac{1}{2}}\mathbf{w}^{\mathrm{N}}_{j,k} - \left\{\mathbf{g}(\mathbf{w}^{\mathrm{S}}_{j,k+1}) - \mathbf{g}(\mathbf{w}^{\mathrm{N}}_{j,k})\right\}}{b^+_{j,k+\frac{1}{2}} - b^-_{j,k+\frac{1}{2}}},$$

and the point values at the cell corners are

$$\mathbf{w}^{\mathrm{NE(NW)}}_{j,k} := \bar{\mathbf{w}}_{j,k}(t) \pm \frac{\Delta x}{2}(\mathbf{w}_x)_{j,k} + \frac{\Delta y}{2}(\mathbf{w}_y)_{j,k},$$

$$\mathbf{w}^{\mathrm{SE(SW)}}_{j,k} := \bar{\mathbf{w}}_{j,k}(t) \pm \frac{\Delta x}{2}(\mathbf{w}_x)_{j,k} - \frac{\Delta y}{2}(\mathbf{w}_y)_{j,k}.$$

REFERENCES

[1] C. BERTHON, M. BREUSS, AND M.-O. TITEUX, *A relaxation scheme for the approximation of the pressureless Euler equations*, Numer. Methods Partial Differential Equations, 22 (2006), pp. 484–505.

[2] F. BOUCHUT, *On zero pressure gas dynamics*, in Advances in Kinetic Theory and Computing, World Scientific, River Edge, NJ, 1994, pp. 171–190.

[3] F. BOUCHUT AND G. BONNAUD, *Numerical simulation of relativistic plasmas in hydrodynamic regime*, Z. Angew. Math. Mech., 76 (1996), pp. 287–290.

[4] F. BOUCHUT AND F. JAMES, *Duality solutions for pressureless gases, monotone scalar conservation laws, and uniqueness*, Comm. Partial Differential Equations, 24 (1999), pp. 2173–2189.

[5] F. BOUCHUT, S. JIN, AND X. LI, *Numerical approximations of pressureless and isothermal gas dynamics*, SIAM J. Numer. Anal., 41 (2003), pp. 135–158.

[6] Y. BRENIER AND E. GRENIER, *Sticky particles and scalar conservation laws*, SIAM J. Numer. Anal., 35 (1998), pp. 2317–2328.

[7] G.-Q. CHEN AND H. LIU, *Formation of δ-shocks and vacuum states in the vanishing pressure limit of solutions to the Euler equations for isentropic fluids*, SIAM J. Math. Anal., 34 (2003), pp. 925–938.

[8] W. E, YU. G. RYKOV, AND YA. G. SINAI, *Generalized variational principles, global weak solutions and behavior with random initial data for systems of conservation laws arising in adhesion particle dynamics*, Comm. Math. Phys., 177 (1996), pp. 349–380.

[9] K. O. FRIEDRICHS, *Symmetric hyperbolic linear differential equations*, Comm. Pure Appl. Math., 7 (1954), pp. 345–392.

[10] S. GOTTLIEB, C.-W. SHU, AND E. TADMOR, *High order time discretization methods with the strong stability property*, SIAM Rev., 43 (2001), pp. 89–112.

[11] A. KURGANOV AND C.-T. LIN, *On the reduction of numerical dissipation in central-upwind schemes*, Commun. Comput. Phys., 2 (2007), pp. 141–163.

[12] A. KURGANOV, S. NOELLE, AND G. PETROVA, *Semidiscrete central-upwind schemes for hyperbolic conservation laws and Hamilton–Jacobi equations*, SIAM J. Sci. Comput., 21 (2001), pp. 707–740.

[13] A. KURGANOV AND G. PETROVA, *Central schemes and contact discontinuities*, M2AN Math. Model. Numer. Anal., 34 (2000), pp. 1259–1275.

[14] A. KURGANOV AND E. TADMOR, *New high-resolution central schemes for nonlinear conservation laws and convection-diffusion equations*, J. Comput. Phys., 160 (2000), pp. 241–282.

[15] B. VAN LEER, *Towards the ultimate conservative difference scheme,* V. *A second order sequel to Godunov's method*, J. Comput. Phys., 32 (1979), pp. 101–136.

[16] P. D. Lax, *Weak solutions of nonlinear hyperbolic equations and their numerical computation*, Comm. Pure Appl. Math., 7 (1954), pp. 159–193.

[17] R. J. LeVeque, *The dynamics of pressureless dust clouds and delta waves*, J. Hyperbolic Differ. Equ., 1 (2004), pp. 315–327.

[18] H. Nessyahu and E. Tadmor, *Non-oscillatory central differencing for hyperbolic conservation laws*, J. Comput. Phys., 87 (1990), pp. 408–463.

[19] Yu. G. Rykov, *The Numerical Method for Solving the 2-D System of Gas Dynamics without Pressure*, KIAM Preprint 76, Moscow, 1996.

[20] Yu. G. Rykov, *Propagation of singularities of shock wave type in a system of equations of two-dimensional pressureless gas dynamics*, Mat. Zametki, 66 (1999), pp. 760–769 (in Russian); translation in Math. Notes, 66 (1999), pp. 628–635 (2000).

[21] Yu. G. Rykov, *On the nonhamiltonian character of shocks in 2-D pressureless gas*, Boll. Unione Mat. Ital. Sez. B Artic. Ric. Mat. (8), 5 (2002), pp. 55–78.

[22] P. K. Sweby, *High resolution schemes using flux limiters for hyperbolic conservation laws*, SIAM J. Numer. Anal., 21 (1984), pp. 995–1011.

[23] M. Vergassola, B. Dubrulle, U. Frish, and A. Noullez, *Burgers equations, Dervil's staircases and the mass distribution for large scale structures*, Astron. Astophys., 289 (1994), pp. 325–356.

[24] Ya. B. Zeldovich, *Gravitational instability: An approximate theory for large density perturbations*, Astron. Astrophys., 5 (1970), pp. 84–89.